

B-Spline Method and Zonal Grids for Simulations of Complex Turbulent Flows

Arthur G. Kravchenko,^{*,1} Parviz Moin,^{*} and Karim Shariff[†]

^{*}*Department of Mechanical Engineering, Stanford University, Stanford, California 94305;*

[†]*NASA Ames Research Center, Moffett Field, California 94035*

E-mail: Arthur.G.Kravchenko@usa.dupont.com

Received September 21, 1998; revised January 22, 1999

A numerical technique for computations of turbulent flows is described. The technique is based on B-splines and allows grid embedding in physically significant flow regions. Numerical tests, which include solutions of nonlinear advection-diffusion equations and computations of flow over a circular cylinder at Reynolds numbers up to 300, indicate that the method is accurate and efficient. In computations of flow over a cylinder, the lift, drag, and base suction coefficients agree well with existing experimental data and previous numerical simulations. © 1999 Academic Press

Key Words: zonal grids; turbulence simulations; Galerkin B-spline methods.

1. INTRODUCTION

Numerical computations of turbulent flows require accurate treatment of essential flow structures. However, the length scales of these structures can vary significantly throughout the computational domain. For example, near-wall eddies in wall-bounded turbulent flows are small compared to the overall flow dimensions but play an important role in the dynamics of turbulent boundary layers. These structures require fine resolution in all three directions near the wall. In large eddy simulation, the near-wall small structures are the important large eddies that cannot be treated accurately with current subgrid-scale parameterizations [1]. Instead, they need to be resolved or completely modeled with dynamic wall treatments [2–4]. In typical computations of wall-bounded turbulent flows, the fine grid resolution in the near-wall region is extended into the outer layers where it is not required.

Grids with refined resolutions in different parts of the computational domain are also necessary for numerical simulations of complex separated flows. For example, in flow over a bluff body, a fine grid is required to resolve the thin boundary and separating shear layers as well as the turbulent wake. A fine grid is usually not necessary in most of the computational

¹ Current address: Dupont Experimental Station, Wilmington, DE 19880.

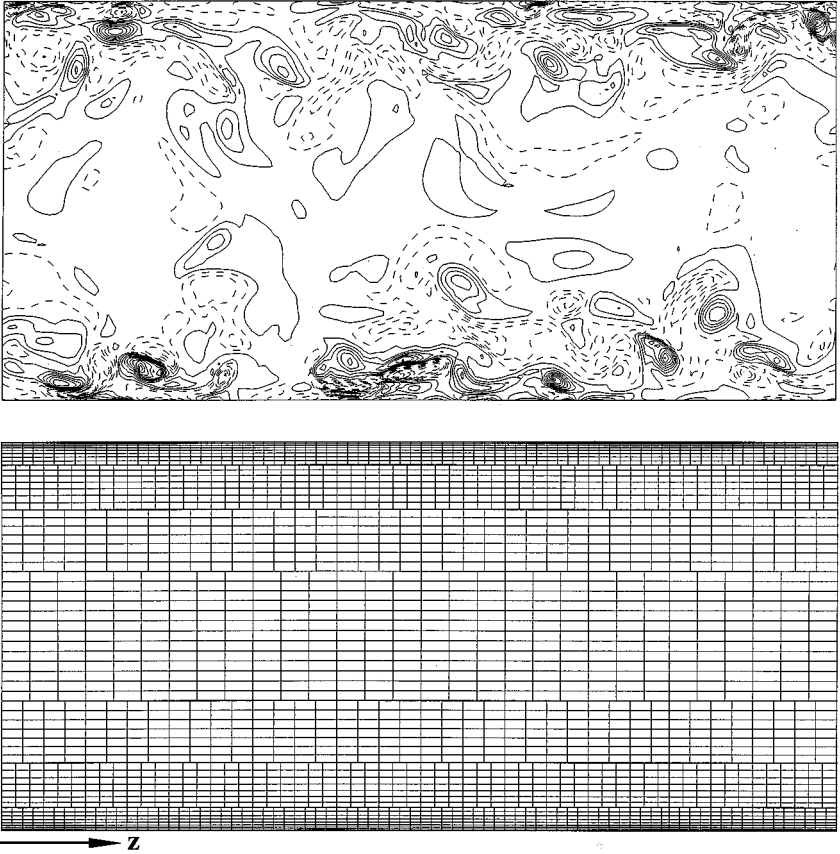


FIG. 1. Streamwise vorticity contours (negative are dashed) in a fully developed turbulent channel flow. The mean flow is into the page. Also shown is the zonal embedded mesh with fine grid near the walls and coarse grid in the middle of the channel.

domain, for instance, in the region upstream of the body where the flow is relatively smooth.

Efficient grid refinement in the physically significant flow regions can be implemented with zonal embedded grids. In this approach, the mesh consists of coarse and fine grid regions (zones), constructed such that appropriate resolution is provided in different parts of the computational domain. This reduces the total number of grid points and leads to savings in CPU time and memory. At the zonal boundaries, the mesh size changes in steps, providing flexibility in designing grids. Figure 1 shows an example of a zonal embedded grid with the mesh size decreasing in steps as one approaches the wall. Such a grid can be used to resolve streamwise vortical structures and wall-layer streaks in the near-wall region of turbulent boundary layers.

Several studies have been undertaken to develop numerical techniques with grid embedding for computations of compressible [5–7] and incompressible [8, 9] flows. Some of these techniques were applied to large eddy simulations [10, 11]. In most of the cases, the techniques were based on low-order finite volume methods with high-order accurate interpolation procedure for exchange of information between zones, and a special treatment of the internal grid boundaries for mass, momentum, and energy conservation. Besides having to deal with the problems of zonal boundary interpolation and conservation [7], in

computations of turbulent flows, these low-order methods may also suffer from significant numerical errors that can overwhelm the effect of subgrid-scale models. The errors can be especially pronounced on zonal grids with large variations in mesh sizes. A quantitative analysis of discretization errors in large eddy simulations has been performed recently by Ghosal [12] who showed that low-order finite-difference schemes might have numerical errors of the same order of magnitude as the subgrid-scale terms. The findings of Ghosal [12] were confirmed numerically in the studies of Lund and Kaltenbach [13] and Kravchenko and Moin [14]. Lund and Kaltenbach [13] used explicit grid filtering to control numerical errors in large eddy simulations of turbulent channel flow at high Reynolds number with a second-order central finite-difference scheme. The smallest scales that would be mostly affected by numerical errors were simply removed from the simulations at every time step. The results were clearly improved but the grid, and therefore the cost of simulations, had to be increased significantly to discern the effect of explicit grid filtering. Kravchenko and Moin [14] performed a series of large eddy simulations of turbulent channel flow to investigate effects of numerical errors in finite-difference schemes of various orders. It was found that, in some cases, the results obtained with the second-order finite-difference scheme were virtually the same with and without a subgrid-scale model, which is not a satisfactory outcome. In contrast, simulations with a 6th-order Padé scheme were significantly improved when the subgrid-scale model was activated.

The studies mentioned above point to the need for the development of high-order non-dissipative numerical schemes that can be used with zonal embedded grids. Nonlinear numerical stability considerations require such schemes to be kinetic energy conserving [14]. However, it is difficult to construct fully conservative finite-difference schemes. The popular staggered mesh scheme for incompressible flows [15, 16] is an example of a fully conservative scheme. A recent work by Morinishi *et al.* [17] has produced a fourth-order conservative scheme.

The objective of the current study is to develop an efficient, accurate, and conservative numerical technique for simulation of turbulent flows in complex geometries on zonal embedded grids. To achieve this objective, we have extended the numerical methodology based on B-splines developed by Kravchenko *et al.* [18] to computations of flows with more than one inhomogeneous direction. The present grid embedding is based on the technique suggested by Shariff and Moser [19]. The resulting numerical methodology is accurate, conservative, and free of aliasing errors. It also offers a greater flexibility for simulations on zonal embedded grids.

2. NUMERICAL METHOD

2.1. Galerkin Method Based on B-Splines in Two Directions

Consider a two-dimensional body with body-fitted coordinates (ξ, η) in the (x, y) plane. Let the velocity vector, \mathbf{u} , be represented in terms of two distinct classes of divergence-free vectors which is equivalent to independently representing two components of the velocity vector with the third determined by the continuity equation,

$$\mathbf{u}(\xi, \eta, z, t) = \sum_{k_z} \sum_m [\hat{\alpha}_m^+(t, k_z) \mathbf{q}_{m, k_z}^+(\xi, \eta, z) + \hat{\alpha}_m^-(t, k_z) \mathbf{q}_{m, k_z}^-(\xi, \eta, z)], \quad (1)$$

where k_z is the spanwise wave number. The method of divergence-free expansions was developed by Leonard and Wray [20]. The expansion vectors $\mathbf{q}^\pm(\xi, \eta, z)$ belong to the

space \mathcal{V} defined as

$$\mathcal{V} = \{\mathbf{q} : \mathbf{q} \in (H^1(\Omega))^3, \nabla \cdot \mathbf{q} = 0\},$$

where Ω is an open set in \mathcal{R}^3 with boundary $\partial\Omega$, and $(H^1(\Omega))^3$ is the Hilbert space defined by

$$(H^1(\Omega))^3 = \{f : f \in (L_2(\Omega))^3, \nabla f \in (L_2(\Omega))^3\}.$$

$(L_2(\Omega))^3$ is the space of square-integrable functions defined on Ω with inner product,

$$(f, g) = \int_{\Omega} fg \, d\Omega \quad \forall f, g \in L_2(\Omega),$$

and norm

$$\|f\| = (f, f)^{\frac{1}{2}} \quad \forall f \in L_2(\Omega).$$

Furthermore, let us choose two classes of weight vectors $\psi^{\pm}(\xi, \eta, z)$ belonging to the space \mathcal{W} defined as

$$\mathcal{W} = \{\psi : \psi \in (H^1(\Omega))^3, \nabla \cdot \psi = 0, \psi = 0 \text{ on } \partial\Omega\}.$$

Following the standard weighted residual approach, we obtain a weak form of the Navier-Stokes equations,

$$\int_{\Omega} \psi^{\pm} \cdot \frac{\partial \mathbf{u}}{\partial t} \, d\Omega = \int_{\Omega} \psi^{\pm} \cdot (\mathbf{H} - \nabla p) \, d\Omega - \frac{1}{Re} \int_{\Omega} (\nabla \times \psi^{\pm}) \cdot (\nabla \times \mathbf{u}) \, d\Omega, \quad (2)$$

where \mathbf{H} denotes the nonlinear term, P is pressure, and the last term is modified using integration by parts and the identity

$$\nabla^2 \mathbf{u} = -\nabla \times \nabla \times \mathbf{u}, \quad (3)$$

which is valid for \mathbf{u} satisfying $\nabla \cdot \mathbf{u} = 0$. Note that the boundary terms resulting from the integration by parts are zero since $\psi = 0$ on $\partial\Omega$. Using the properties of the weight functions, $\nabla \cdot \psi = 0$ on Ω and $\psi = 0$ on $\partial\Omega$, we can eliminate the pressure term (after integration by parts) from the weak formulation (2) to obtain

$$\int_{\Omega} \left[\psi^{\pm} \cdot \left(\frac{\partial \mathbf{u}}{\partial t} - \mathbf{H} \right) + \frac{1}{Re} (\nabla \times \psi^{\pm}) \cdot (\nabla \times \mathbf{u}) \right] \, d\Omega = 0. \quad (4)$$

2.2. Weight and Expansion Functions

The expansion functions can be chosen as

$$\mathbf{q}_{m,k_z}^+(\xi, \eta, z) = \nabla \times \begin{pmatrix} 0 \\ 0 \\ B_m(\xi, \eta) \end{pmatrix} e^{ik_z z}, \quad (5a)$$

$$\mathbf{q}_{m,k_z}^-(\xi, \eta, z) = \nabla \times \begin{pmatrix} \frac{y_j}{J} B_m(\xi, \eta) \\ -\frac{x_j}{J} B_m(\xi, \eta) \\ 0 \end{pmatrix} e^{ik_z z}. \quad (5b)$$

Satisfaction of the divergence-free restriction on \mathbf{q} is guaranteed by the identity $\nabla \cdot \mathbf{q} = \nabla \cdot (\nabla \times \Psi) = 0$. $B_m(\xi, \eta)$ for $m = 1 \dots M$ are the two-dimensional B-splines for the given zonal mesh. Each $B_m(\xi, \eta)$ is a product of one-dimensional B-splines in the directions ξ and η ,

$$B_m(\xi, \eta) = f_i(\xi)g_j(\eta),$$

where index m corresponds to two-dimensional functions, and i and j are the indices for one-dimensional B-splines. One-dimensional B-splines, $f_i(\xi)$ of degree k are defined on a set of $(N_\xi + 1)$ knot points $[t_0, t_1, \dots, t_{N_\xi}]$ by the following recursive relationship [21],

$$f_i^k(\xi) = \frac{(\xi - t_{i-k-1})}{(t_{i-1} - t_{i-k-1})} f_{i-1}^{k-1}(\xi) + \frac{(t_i - \xi)}{(t_i - t_{i-k})} f_i^{k-1}(\xi), \quad i = 1, \dots, N_\xi + k, \quad (6)$$

where a B-spline of degree zero is a top hat function, i.e., $f_i^0(\xi) = 1$ if $t_{i-1} \leq \xi \leq t_i$ and 0 otherwise. One-dimensional B-splines, $g_j(\eta)$, are defined similarly. An example of the quadratic B-splines ($k = 2$) defined on a uniformly spaced set of knot points is shown in Fig. 2.

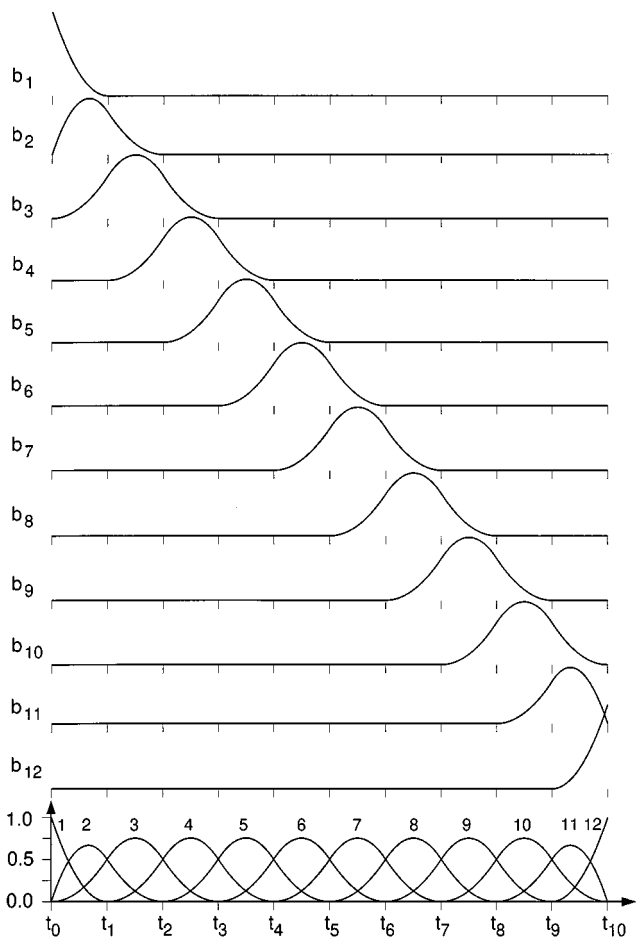


FIG. 2. Twelve second-order B-splines, $b_i(t)$, shown on a uniform 11-point knot set. Knots, t_i , are indicated by short vertical lines. The bottom composite graph is in the form that is useful to display sets of B-splines.

The metric coefficients x_ξ , y_ξ , x_η , and y_η are the derivatives of the generalized coordinate system mapping functions $x(\xi, \eta)$ and $y(\xi, \eta)$ and $J = x_\xi y_\eta - x_\eta y_\xi$ is the Jacobian.

The set of weight vectors is identical to the set of expansion vectors except that in order to satisfy an additional restriction on weight functions, $\psi = 0$ on $\partial\Omega$, those vectors having support on the boundaries are eliminated from the set. The particular choice of the divergence-free vectors, (5), leads to a complete and relatively simple set of basis functions. Different sets can also be used provided that they are complete [20].

Equation (5) can be written as

$$\mathbf{q}_{m,k_z}^+(\xi, \eta, z) = \begin{pmatrix} a_m(\xi, \eta) \\ b_m(\xi, \eta) \\ 0 \end{pmatrix} e^{ik_z z}, \quad (7a)$$

$$\mathbf{q}_{m,k_z}^-(\xi, \eta, z) = \begin{pmatrix} ik_z c_m^a(\xi, \eta) \\ ik_z c_m^b(\xi, \eta) \\ d_m(\xi, \eta) \end{pmatrix} e^{ik_z z}, \quad (7b)$$

where a , b , c^a , c^b , and d are (for brevity, the subscript m is omitted in the following expressions)

$$a(\xi, \eta) = [x_\xi B_\eta(\xi, \eta) - x_\eta B_\xi(\xi, \eta)]/J, \quad (8a)$$

$$b(\xi, \eta) = [y_\xi B_\eta(\xi, \eta) - y_\eta B_\xi(\xi, \eta)]/J, \quad (8b)$$

$$c^a(\xi, \eta) = x_\eta B(\xi, \eta)/J, \quad (8c)$$

$$c^b(\xi, \eta) = y_\eta B(\xi, \eta)/J, \quad (8d)$$

$$d(\xi, \eta) = -B_\eta(\xi, \eta)/J. \quad (8e)$$

2.3. System of Equations

Evaluating the integrals in (4), we obtain the system of ordinary differential equations for each wave number k_z ,

$$\begin{pmatrix} \mathbf{M}^{++} & \mathbf{M}^{+-} \\ \mathbf{M}^{-+} & \mathbf{M}^{--} \end{pmatrix} \frac{d}{dt} \begin{pmatrix} \hat{\alpha}^+ \\ \hat{\alpha}^- \end{pmatrix} = - \begin{pmatrix} \hat{\mathbf{R}}^+(\alpha^+, \alpha^-) \\ \hat{\mathbf{R}}^-(\alpha^+, \alpha^-) \end{pmatrix} - \frac{1}{Re} \begin{pmatrix} \mathbf{D}^{++} & \mathbf{D}^{+-} \\ \mathbf{D}^{-+} & \mathbf{D}^{--} \end{pmatrix} \begin{pmatrix} \hat{\alpha}^+ \\ \hat{\alpha}^- \end{pmatrix}, \quad (9)$$

where $\hat{\cdot}$ indicates a Fourier transform and $\mathbf{M}^{\pm\pm}$ and $\mathbf{D}^{\pm\pm}$ are the mass and viscous matrices. Due to de-coupling in the z -direction only matrices for two-dimensional operators have to be stored. However, each \mathbf{M} or \mathbf{D} matrix may involve a linear combination of up to three such matrices, e.g.,

$$\mathbf{M}^{--} = \mathbf{M}_1 - k_z^2 \mathbf{M}_2, \quad (10)$$

where matrices \mathbf{M}_1 and \mathbf{M}_2 are independent of k_z . $\hat{\mathbf{R}}^\pm(\alpha^+, \alpha^-)$ are the expressions for the nonlinear terms. Complete expressions for the mass and viscous matrices and components

of the nonlinear terms are given in the Appendix. The components of mass, viscous, and nonlinear matrices are computed and stored prior to time advancement. Generally, the metrics and Jacobian functions in the expressions for \mathbf{q} and ψ are not piecewise polynomials and the integrals in (4) cannot be evaluated exactly. In our computations, such functions were treated as if they were polynomials of high degree (at least 8) on each integration interval. The system of ordinary differential equations (9) can be solved for the B-spline expansion coefficients α^+ and α^- with a standard time-stepping algorithm. In our study, the time advancement is performed with Crank–Nicolson and third-order Runge–Kutta schemes for the viscous and advection terms, respectively. The mass and viscous matrices are symmetric and positive definite and, therefore, a conjugate gradient method can be used for the iterative solution of the resulting linear system of equations at each time step.

2.4. *Nonlinear Terms*

The expressions for $\hat{\mathbf{R}}^\pm(\alpha^+, \alpha^-)$ result from the integration of the products of weight functions with the nonlinear terms in Eq. (4). To avoid the high computational cost associated with evaluation of the convolution sums in Fourier space, the nonlinear terms are computed in the B-spline/ z physical space. Thus, the B-spline coefficients in the velocity expansions are transformed from Fourier to physical space using the “3/2 rule” [22] for de-aliasing. The expressions for all the nonlinear terms are shown in the Appendix. To illustrate the computation of $\hat{\mathbf{R}}^\pm(\alpha^+, \alpha^-)$, we consider a sample nonlinear term arising in the z momentum equation,

$$\mathbf{N}_{ij} = \int_{\Omega_\xi} \int_{\Omega_\eta} f_i(\xi) g'_j(\eta) u_3^2 d\xi d\eta, \tag{11}$$

where u_3 is the spanwise component of velocity. Substituting the expansion for u_3 one obtains

$$\mathbf{N}_{ij} = \sum_{klmn} N_{ijklmn} \alpha_{kl}^- \alpha_{mn}^-, \tag{12}$$

where

$$N_{ijklmn} = \int_{\Omega_\xi} \int_{\Omega_\eta} \frac{1}{J^2(\xi, \eta)} f_i g'_j f_k g'_l f_m g'_n d\xi d\eta. \tag{13}$$

All nonlinear matrices have the same structure (pattern of non-zero elements) as (12) and are pre-computed and stored prior to the time advancement. Here, we are using the term “matrix” in a generalized sense to refer to a multi-indexed quantity. The number of operations required for computing (12) is proportional to $(2k + 1)^4 N_\alpha$ where k is the degree of the B-splines and N_α is the total number of two-dimensional B-splines. This estimate for the operation count is simply the number of elements in the nonlinear matrix: its structured part has $(2k + 1)^4$ diagonals with N_α entries in each. Even though the number of operations is linear in N_α , the cost associated with computations of the nonlinear term can be very high, especially for high-degree B-splines due to the large coefficient, $(2k + 1)^4$. In typical simulations with second-degree B-splines ($k = 2$), more than 50% of the CPU time is spent in evaluating the nonlinear terms.

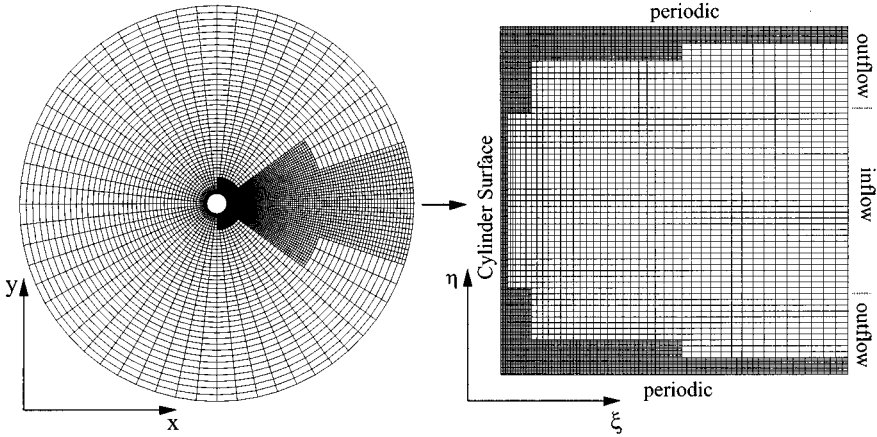


FIG. 3. An example of zonal grid in a generalized coordinate system for computations of flow over a cylinder mapped onto a rectangular grid in ξ and η . Also shown are locations of the periodic, inflow, and outflow boundary conditions.

2.5. Boundary Conditions

One of the test problems chosen to assess the performance of the B-spline technique on zonal grids is a two-dimensional flow over a circular cylinder. Therefore, we will describe in detail the boundary conditions for this test case. The extension to three-dimensional flow and other two-dimensional body shapes is straightforward.

The simulations of two-dimensional flow over a cylinder are carried out on an O-type zonal mesh which is mapped to a rectangular domain ($0 \leq \xi \leq 1$, $0 \leq \eta \leq 1$). An example of a typical grid, but with domain size smaller than the one actually used, is shown in Fig. 3. For the two-dimensional case, the spanwise component of velocity and, therefore, the coefficients $\alpha_{i,j}^-$ are zero. The streamwise (x) and cross-flow (y) velocity components are represented as

$$u(\xi, \eta) = \sum_{i,j} \alpha_{i,j}^+ [x_\xi f_i(\xi) g'_j(\eta) - x_\eta f'_i(\xi) g_j(\eta)] / J, \quad (14)$$

$$v(\xi, \eta) = \sum_{i,j} \alpha_{i,j}^+ [y_\xi f_i(\xi) g'_j(\eta) - y_\eta f'_i(\xi) g_j(\eta)] / J.$$

Non-slip boundary conditions are imposed at the cylinder surface,

$$u(\xi = 0, \eta) = v(\xi = 0, \eta) = 0. \quad (15)$$

Constant potential flow boundary conditions are used at the inflow ($0.25 \leq \eta \leq 0.75$),

$$u = U_{\text{potential}}, \quad (16a)$$

$$v = V_{\text{potential}}, \quad (16b)$$

and convective boundary conditions are applied at the outflow portion of the outer boundary

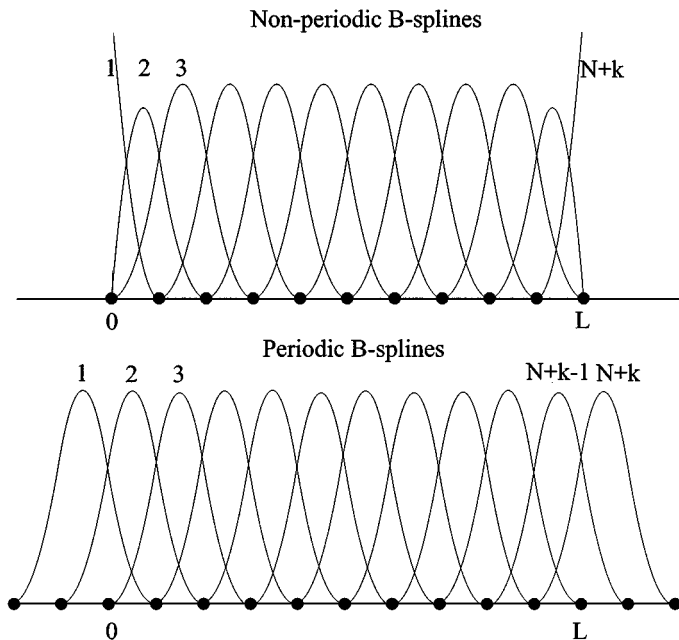


FIG. 4. Composite graph of non-periodic and periodic B-splines (see Fig. 2) of order 2 on domain $0 \leq \eta \leq L$; N is number of grid intervals; in case of periodic B-splines, $g_1 \equiv g_{N+k-1}$ and $g_2 \equiv g_{N+k}$.

$(0.0 \leq \eta \leq 0.25, 0.75 \leq \eta \leq 1.0)$,

$$\frac{\partial u}{\partial t} + U_\infty \frac{1}{J} \left(y_\eta \frac{\partial u}{\partial \xi} - y_\xi \frac{\partial u}{\partial \eta} \right) = 0, \tag{17a}$$

$$\frac{\partial v}{\partial t} + U_\infty \frac{1}{J} \left(y_\eta \frac{\partial v}{\partial \xi} - y_\xi \frac{\partial v}{\partial \eta} \right) = 0. \tag{17b}$$

An explicit third-order Runge–Kutta scheme is used to advance Eq. (17) in time.

Periodic boundary conditions are used at $\eta = 0$ and $\eta = 1$. Periodicity is implemented by extending the computational domain in η and creating additional B-splines at one boundary that are equivalent to the B-splines at the other one, as shown in Fig. 4. The matrices in Eq. (9) are then modified to account for periodicity.

Consider boundary conditions at $\xi = 0$ and $\xi = 1$. At these boundaries, Eqs. (14) become

$$u(0, \eta) = \sum_{i,j} \alpha_{i,j}^+ [x_\xi f_i(0)g'_j(\eta) - x_\eta f'_i(0)g_j(\eta)]/J, \tag{18}$$

$$v(0, \eta) = \sum_{i,j} \alpha_{i,j}^+ [y_\xi f_i(0)g'_j(\eta) - y_\eta f'_i(0)g_j(\eta)]/J,$$

$$u(1, \eta) = \sum_{i,j} \alpha_{i,j}^+ [x_\xi f_i(1)g'_j(\eta) - x_\eta f'_i(1)g_j(\eta)]/J, \tag{19}$$

$$v(1, \eta) = \sum_{i,j} \alpha_{i,j}^+ [y_\xi f_i(1)g'_j(\eta) - y_\eta f'_i(1)g_j(\eta)]/J.$$

The only B-splines which have non-zero values at $\xi = 0$ and $\xi = 1$ are $f_1(0)$ and $f_{N_\xi}(1)$. The only non-zero first derivatives at $\xi = 0$ and $\xi = 1$ are $f'_1(0)$, $f'_2(0)$, $f'_{N_\xi-1}(1)$, and $f'_{N_\xi}(1)$.

With these simplifications, Eqs. (18) and (19) become

$$\begin{aligned} y_\eta u(0, \eta) - x_\eta v(0, \eta) &= \sum_j \alpha_{1,j}^+ f_1(0) g_j'(\eta), \\ y_\eta u(1, \eta) - x_\eta v(1, \eta) &= \sum_j \alpha_{N_\xi, j}^+ f_{N_\xi}(1) g_j'(\eta), \end{aligned} \quad (20)$$

$$\begin{aligned} y_\xi u(0, \eta) - x_\xi v(0, \eta) &= \sum_j \alpha_{1,j}^+ f_1'(0) g_j(\eta) + \sum_j \alpha_{2,j}^+ f_2'(0) g_j(\eta), \\ y_\xi u(1, \eta) - x_\xi v(1, \eta) &= \sum_j \alpha_{N_\xi, j}^+ f_{N_\xi}'(1) g_j(\eta) + \sum_j \alpha_{N_\xi-1, j}^+ f_{N_\xi-1}'(1) g_j(\eta). \end{aligned} \quad (21)$$

Multiplying Eq. (20) by $g_k'(\eta)$ and Eq. (21) by $g_k(\eta)$ and integrating, we obtain a linear system of equations from which coefficients $\alpha_{1,j}^+$, $\alpha_{2,j}^+$, $\alpha_{N_\xi-1, j}^+$, and $\alpha_{N_\xi, j}^+$ can be determined. However, the coefficients $\alpha_{1,j}^+$ and $\alpha_{N_\xi, j}^+$ obtained from Eq. (20) are not unique. Since the sum of the B-spline derivatives is zero [21],

$$\sum_j g_j'(\eta) = 0,$$

addition of constants C_1 and C_2 to the coefficients $\alpha_{1,j}^+$ and $\alpha_{N_\xi, j}^+$ does not change the values of velocities at the boundaries. The physical interpretation is that $C_2 - C_1$ represents the constant up to which the flux function, $F(\eta) \equiv \int_0^1 u^{(\xi)} d\xi$, is determined ($u^{(\xi)}$ is the velocity in the ξ -direction). This can be shown by considering the stream function. The stream function, Ψ , is defined by

$$\mathbf{u} = \nabla \times \begin{pmatrix} 0 \\ 0 \\ \Psi \end{pmatrix},$$

and, therefore,

$$\Psi(\xi, \eta) = \sum_{i,j} \alpha_{i,j}^+ f_i(\xi) g_j(\eta). \quad (22)$$

At the boundaries,

$$\begin{aligned} \Psi(0, \eta) &= \sum_j \alpha_{1,j}^+ f_1(0) g_j(\eta), \\ \Psi(1, \eta) &= \sum_j \alpha_{N_\xi, j}^+ f_{N_\xi}(1) g_j(\eta), \end{aligned}$$

where $f_1(0) = f_{N_\xi}(1) = 1$ according to the B-spline definitions. The flux function, $F(\eta)$, is related to the stream function at the boundaries by

$$F(\eta) = \Psi(1, \eta) - \Psi(0, \eta) = \sum_j (\alpha_{N_\xi, j}^+ - \alpha_{1,j}^+) g_j(\eta). \quad (23)$$

Different expansion coefficients, $\alpha_{N_\xi, j}^+ + C_2$ and $\alpha_{1,j}^+ + C_1$, produce different flux functions,

$$\check{F}(\eta) = \check{\Psi}(1, \eta) - \check{\Psi}(0, \eta) = \sum_j (\alpha_{N_\xi, j}^+ + C_2 - (\alpha_{1,j}^+ + C_1)) g_j(\eta),$$

or

$$\check{F}(\eta) = \check{\Psi}(1, \eta) - \check{\Psi}(0, \eta) = C_2 - C_1 + \sum_j (\alpha_{N_\xi, j}^+ - \alpha_{1, j}^+) g_j(\eta), \tag{24}$$

since

$$\sum_j g_j(\eta) = 1.$$

Clearly, the two flux functions, $F(\eta)$ and $\check{F}(\eta)$, differ from each other by the constant, $C_2 - C_1$. One of the constants, C_2 or C_1 , can be chosen arbitrarily. This corresponds to the freedom of choosing a constant up to which the stream function is defined. Once one constant is chosen, the other one must be determined as part of the solution. Of several possible approaches, the one presently followed is to set the other constant arbitrarily as well and to free the constraint thus imposed by introducing an additional divergence-free function which is added to the set of expansion and weight functions. Then, the velocity representation becomes

$$\begin{aligned} u(\xi, \eta) &= \sum_{i,j} \alpha_{ij}^+ [x_\xi f_i(\xi) g'_j(\eta) - x_\eta f'_i(\xi) g_j(\eta)]/J - \beta(t) x_\eta \mathcal{F}(\xi)/J, \\ v(\xi, \eta) &= \sum_{i,j} \alpha_{ij}^+ [y_\xi f_i(\xi) g'_j(\eta) - y_\eta f'_i(\xi) g_j(\eta)]/J - \beta(t) y_\eta \mathcal{F}(\xi)/J, \end{aligned} \tag{25}$$

where $\mathcal{F}(\xi)$ is an extra function, and β is its coefficient, which is determined as part of the solution together with the rest of the coefficients, α_{ij}^+ . This function, $\mathcal{F}(\xi)$, is chosen to be zero at $\xi = 0$ and $\xi = 1$ and to have non-zero value of $\int_0^1 \mathcal{F}(\xi) d\xi$.

3. ZONAL GRID

3.1. Mesh Definition and Function Selection

A typical zonal mesh with sudden grid resolution changes is shown in Fig. 5. This particular mesh is constructed with two knot sets in y , shown by the solid circles, and two

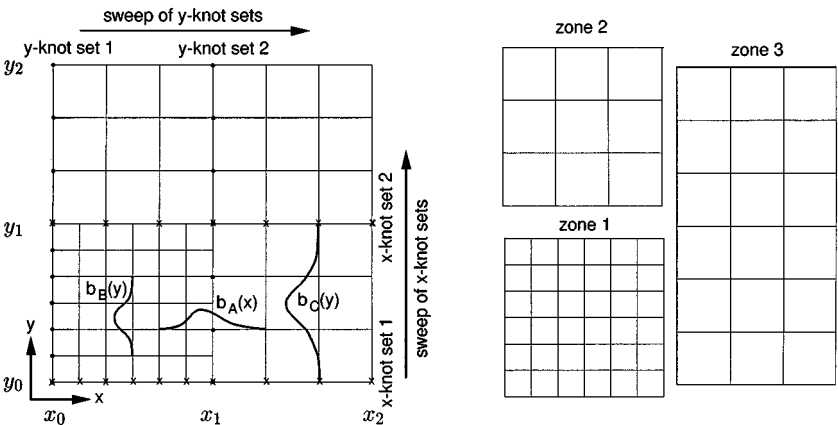


FIG. 5. Construction of two-dimensional B-splines on zonal grid. Symbols \bullet and \times show locations of knot points.

knot sets in x , shown by the x symbol. The knot sets are swept across certain regions to form the lines of the zonal mesh. For example, y -knot set 1 is swept horizontally from x_0 to x_1 and y -knot set 2 is swept from x_1 to x_2 to form the horizontal lines. Similarly, x -knot set 1 and x -knot set 2 are swept vertically from y_0 to y_1 and from y_1 to y_2 , respectively, to form the vertical lines of the mesh. The zonal grid is then disassembled into three zones with regular mesh in both directions of each zone, as shown in Fig. 5. Furthermore, two classes of two-dimensional B-splines are constructed: confined and spilling functions. The support of confined functions resides entirely in a particular zone. The support of spilling functions is allowed to cross zonal boundaries. Two-dimensional *confined* B-spline functions are simply constructed by forming products of one-dimensional B-splines defined on the grids in each direction of a zone. An algorithm for the construction of *spilling* functions is more complicated and is described in detail by Shariff and Moser [19]. As pointed out by Shariff and Moser [19], there is no rigorous mathematical proof that the algorithm gives a complete set of basis functions. Construction of spilling functions is based on finding the products of B-splines in both directions such that no additional grid lines are produced by the supports of these B-splines. For example, the product of the function $b_A(x)$ defined on the x -knot set 1 and the function $b_B(y)$ defined on the y -knot set 1 cannot be chosen as a spilling function because it creates additional horizontal grid lines in zone 3. On the other hand, a product of the function $b_A(x)$ and the function $b_C(y)$ defined on the y -knot set 2 forms a legitimate spilling function. The function $b_C(y)$ is also called a suitable multiplier for the function $b_A(x)$. Our sample zonal grid shown in Fig. 5 gives the following number of two-dimensional quadratic B-spline functions,

$$\begin{aligned} N_{zone1} &= N_{x_1} \times N_{y_1} = 6 \times 6 = 36, \\ N_{zone2} &= N_{x_2} \times N_{y_2} = 3 \times 3 = 9, \\ N_{zone3} &= N_{x_3} \times N_{y_3} = 3 \times 8 = 24, \\ N_c &= 69, \quad N_s = 22, \end{aligned}$$

where N_{zone1} , N_{zone2} , and N_{zone3} are the number of confined functions in zones 1, 2, and 3, respectively. The total number of confined functions is N_c , and N_s gives the number of spilling functions selected on this grid.

Once the confined functions are formed and the spilling functions are selected, a numerical representation of the dependent variable in a problem is

$$\tilde{u}(x, y) = \sum_{i=1}^{N_c} \alpha_i C_i(x, y) + \sum_{i=1+N_c}^{N_s+N_c} \alpha_i S_{i-N_c}(x, y), \quad (26)$$

where $C(x, y)$ and $S(x, y)$ are the confined and spilling functions and N_c and N_s are the numbers of the confined and spilling functions, respectively. For integer refinement ratios across zones, Eq. (26) constitutes a C^{k-1} continuous spline with knot lines coinciding with the mesh. The total number of confined functions is $N_c = \sum_{i_z=1}^{N_{zones}} N_c^{i_z}$, where $N_c^{i_z}$ is the number of confined functions in each grid zone i_z , and N_{zones} is the total number of zones. The total number of degrees of freedom is given by $N_{dof} = N_c + N_s$. This number is related to the number of knot points on a given mesh.

3.2. Implementation of Galerkin B-Spline Method on Zonal Grid

To illustrate the implementation of the two-dimensional Galerkin B-spline method on zonal grid, we consider the following nonlinear convection-diffusion equation,

$$\frac{\partial u}{\partial t} + u \frac{\partial u}{\partial x} = \nu \left(\frac{\partial^2}{\partial x^2} + \frac{\partial^2}{\partial y^2} \right) u, \tag{27}$$

with boundary conditions

$$u(0, y) = u_L(y), \tag{28a}$$

$$u(L_x, y) = u_R(y), \tag{28b}$$

$$u(x, 0) = u_B(x), \tag{28c}$$

$$u(x, L_y) = u_T(x). \tag{28d}$$

The implementation of the Galerkin B-spline method on zonal grid for the Navier–Stokes equations is similar but more cumbersome. The parameter ν in Eq. (27) is the diffusion coefficient. Let us solve Eq. (27) on the zonal grid shown in Fig. 5. Substituting the expansion (26) in Eq. (27) and performing the Galerkin procedure, i.e., multiplying both sides of Eq. (27) by two-dimensional B-splines as weight functions and integrating over the entire computational domain, we obtain a system of ordinary differential equations for the expansion coefficients α :

$$\sum_j m_{ij} \frac{d\alpha_j}{dt} = \nu \sum_j v_{ij} \alpha_j - \sum_j \sum_l n_{ijl} \alpha_j \alpha_l. \tag{29}$$

In matrix form, the system (29) is

$$\mathbf{M} \frac{d\alpha}{dt} = \nu \mathbf{V} \alpha - \mathbf{N}(\alpha, \alpha), \tag{30}$$

where \mathbf{M} and \mathbf{V} are linear mass and diffusion matrices and $\mathbf{N}(\alpha, \alpha)$ is the nonlinear term. The elements of the linear and nonlinear matrices are given by

$$\begin{aligned} m_{ij} &= \int_{\Omega_x} \int_{\Omega_y} B_i(x, y) B_j(x, y) dx dy, \\ v_{ij} &= \int_{\Omega_x} \int_{\Omega_y} \left(B_i(x, y) \frac{\partial^2 B_j}{\partial x^2}(x, y) + B_i(x, y) \frac{\partial^2 B_j}{\partial y^2}(x, y) \right) dx dy, \\ n_{ijl} &= \int_{\Omega_x} \int_{\Omega_y} B_i(x, y) B_j(x, y) \frac{\partial B_l}{\partial x}(x, y) dx dy. \end{aligned}$$

The form of the linear matrix is shown in Fig. 6. This particular matrix corresponds to the Galerkin method based on B-splines of second degree defined on the zonal grid of Fig. 5. The elements in the unstructured part of the linear matrix result from the interactions between two spilling functions or between spilling and confined functions. The functions interact if their supports overlap, in which case the integral of the product of these functions is non-zero. The number of different interactions is given in Table I. Only interactions between different

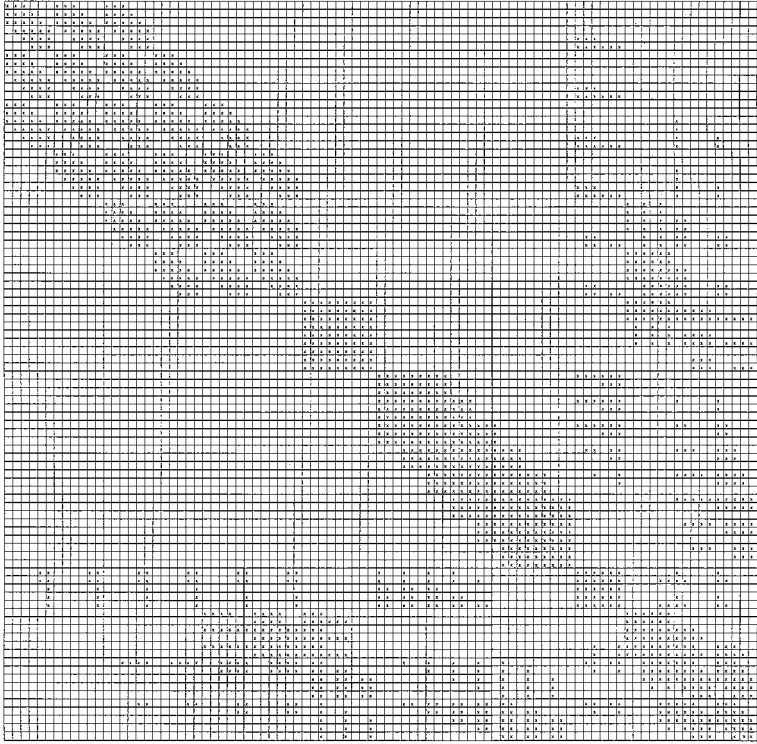


FIG. 6. Two-dimensional matrix resulting from zonal grid. Symbols \times show locations of non-zero elements.

functions are recorded. However, each spilling function can interact with itself. Such an interaction corresponds to the diagonal element in the unstructured part of the linear matrix. The total number of unstructured elements is $N_{us} = 2(N_{ss} + N_{sc}) + N_s$. The three structured parts of the matrix correspond to the three zones of the zonal grid of Fig. 5. Each part has a form of a block-multidiagonal matrix with the elements formed from the interactions of the confined functions in the zones. It is convenient to store the structured parts of linear matrices for each zone by diagonals. The gaps in the diagonals are filled with zeros in order to simplify the implementation. For each diagonal, we store all the elements, the number of entries in the diagonal, and the row and column of the first element in each diagonal. The number of diagonals in the structured part of a linear matrix depends on the degree of B-splines, k , and is equal to $(2k + 1)^2$. For example, the structured parts of the matrix in Fig. 6 have 25 diagonals ($25 = (2 \cdot 2 + 1)^2$). The row and column of the first element of

TABLE I
Number of Interactions between Two-Dimensional B-Splines of Degree 2
Defined on Zonal Grid of Fig. 5

$N_{ss} = 100$	Number of interactions between spilling functions
$N_{sc} = 297$	Number of interactions between spilling and confined functions
$N_{sss} = 209$	Number of triple interactions between spilling functions
$N_{ccs} = 776$	Number of triple interactions between 2 confined and 1 spilling functions
$N_{css} = 778$	Number of triple interactions between 1 confined and 2 spilling functions

each diagonal are given by

$$\begin{aligned}\text{row}_{i,j,n} &= 1 - \min(i, 0) - \min(j, 0) \cdot N_{x_n}, \\ \text{column}_{i,j,n} &= 1 - \min(i, 0) + i - (\min(j, 0) - j) \cdot N_{x_n},\end{aligned}$$

where $-k \leq i, j \leq k$, n is the grid zone index and N_{x_n} is the number of B-splines in the x -direction of zone n .

A so-called nonlinear matrix, corresponding to the nonlinear term, is formed from interactions between three two-dimensional B-splines. The nonlinear matrix consists of structured and unstructured parts. Unstructured elements of a nonlinear matrix are formed from interactions among either three spilling functions, 2 confined and 1 spilling functions, or 1 confined and 2 spilling functions. The total number of unstructured elements in the nonlinear matrix of Eq. (30) is $N_{usq} = 6(N_{ss} + N_{sc} + N_{sss} + N_{ccs} + N_{css}) + N_s$, where the factor 6 is used to account for the symmetric interactions (interaction between a confined function, $C(x, y)$, and a spilling function, $S(x, y)$, is the same as that between $S(x, y)$ and $C(x, y)$ —this interaction is called symmetric). Note that N_{ss} and N_{sc} are present in the definition of N_{usq} . These are used to account for interactions in which two functions are the same and the third is different. For example, an interaction that involves a spilling function counted twice and a confined function will contribute an element to the unstructured part of the nonlinear matrix and is accounted for in the second term of N_{usq} . The number of different unstructured interactions for the zonal grid of Fig. 5 is given in Table I. The structured part of a nonlinear matrix is also similar to that of a linear matrix and consists of multidagonal blocks. The row, column, and depth of the first element of each diagonal in every block are given by

$$\begin{aligned}\text{row}_{i_1, j_1, i_2, j_2, izone} &= 1 - \min(i_1, j_1, 0) - \min(i_2, j_2, 0) \cdot N_{x_{izone}}, \\ \text{column}_{i_1, j_1, i_2, j_2, izone} &= 1 - \min(i_1, j_1, 0) + i_1 - (\min(i_2, j_2, 0) - i_2) \cdot N_{x_{izone}}, \\ \text{depth}_{i_1, j_1, i_2, j_2, izone} &= 1 - \min(i_1, j_1, 0) + j_1 - (\min(i_2, j_2, 0) - j_2) \cdot N_{x_{izone}},\end{aligned}$$

where $-k \leq i_1, i_2 \leq k$, $\max(-k, -k + i_1) \leq j_1 \leq \min(k, k + i_1)$ and $\max(-k, -k + i_2) \leq j_2 \leq \min(k, k + i_2)$.

The boundary conditions, (28), are imposed strongly by determining the values of the expansion coefficients corresponding to non-zero boundary B-splines. Thus, the boundary condition (28a) is

$$\tilde{u}(0, y) = \sum_{i=1}^{N_c} \alpha_i C_i(0, y) + \sum_{i=1+N_c}^{N_s+N_c} \alpha_i S_{i-N_c}(0, y) = u_L(y).$$

Both confined and spilling functions at the boundary, $x = 0$, will have 1D B-splines defined on the knot set of this boundary as one of their multipliers. The boundary expansion coefficients are then determined from

$$\tilde{u}(0, y) = \sum_{i=1}^{N_b} \alpha_j b_j(y) = u_L(y), \quad (31)$$

where $b_j(y)$ are the B-splines defined on a knot set at $x = 0$, and N_b is the number of these B-splines. Expansion coefficients, α_j , in (31) are obtained by B-spline projection.

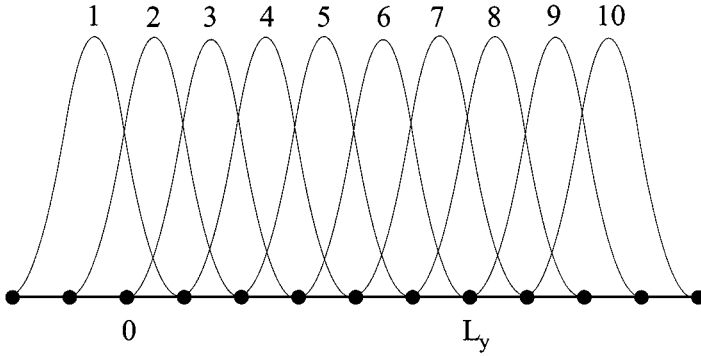


FIG. 7. Periodic B-splines on extended domain. Here, $b_1(y) \equiv b_7(y)$, $b_2(y) \equiv b_8(y)$, $b_3(y) \equiv b_9(y)$, and $b_4(y) \equiv b_{10}(y)$.

In problems with periodic boundary conditions, linear matrices are modified to account for the periodicity of the expansion coefficients. Consider, for example, a single-zone 5×7 grid on which the second direction is periodic. The number of second-degree B-splines defined on this grid is $6 \times 8 = 48$. However, as we saw above, some of the B-splines in the second direction will be equivalent, i.e., $b_1(y) \equiv b_7(y)$ and $b_2(y) \equiv b_8(y)$. For simplicity in implementation, it is useful to introduce 2 (or k for a general k -degree B-spline) additional knot points at one end of the periodic direction so that $b_3(y) \equiv b_9(y)$ and $b_4(y) \equiv b_{10}(y)$ as shown in Fig. 7. A linear matrix corresponding to the new set of 6×10 B-splines is shown on the top of Fig. 8. This matrix is modified to account for the equivalence of the B-splines and corresponding expansion coefficients, as shown on the bottom of Fig. 8. The matrix entries corresponding to the B-splines, $b_1(y)$, $b_2(y)$, $b_9(y)$, and $b_{10}(y)$ are set to zero except for the diagonal elements which are set to one to ensure that the matrix is nonsingular. The resulting matrix is periodic and guarantees the periodicity of the expansion coefficients. Once the matrix is inverted, the expansion coefficients corresponding to the boundary B-splines are obtained from periodicity.

4. NUMERICAL TESTS

4.1. Accuracy of Galerkin B-Spline Method

The accuracy of a numerical technique based on piecewise polynomials, such as B-splines, has been studied in the past [23]. For example, it has been shown that, for a method based on B-splines of a particular order k , the convergence rate of L_2 errors of numerical solutions is equal to $k + 1$, where the L_2 error norm is estimated as

$$L_2 \text{ error norm} = \left(\int_{\Omega} (u_{\text{exact}}(x) - u_{\text{numer}}(x))^2 dx \right)^{\frac{1}{2}}.$$

Convergence studies for two-dimensional problems solved with B-spline-based methods are given in Ref. [19].

One of the better criteria for the accuracy evaluation of a numerical method is its modified wave number curve. Such a curve shows numerical errors versus wave numbers in the solution and, therefore, demonstrates the suitability of a numerical technique for computations of problems with a broad spectrum such as in a turbulent flow.

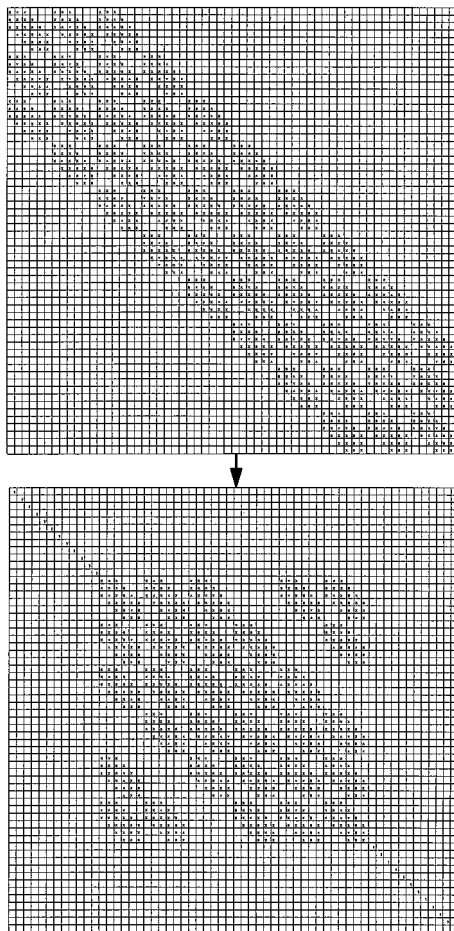


FIG. 8. Construction of periodic two-dimensional matrix. Symbols \times show locations of non-zero elements.

Figures 9 and 10 show the modified wave number diagrams for the first and second derivative operators approximated by Galerkin methods with various order B-splines. The curves demonstrate that the methods based on B-splines have very good modified wave number properties which resemble those of the Padé schemes (for modified wave numbers of the compact finite-difference schemes see Ref. [24]). For instance, the Galerkin method with B-splines of order 2 is fairly accurate for about $2/3$ of the wave numbers. The accuracy is always higher for low wave numbers and lower at high wave numbers, especially for the first derivative operators. However, with an increase in the order of B-splines, the accuracy at high wave numbers improves.

4.2. Two-Dimensional Nonlinear Convection-Diffusion Equation

The test problem chosen to assess the performance of the numerical technique with embedding in two inhomogeneous directions is the two-dimensional nonlinear convection-diffusion equation. This is a relatively simple problem that can provide insight into various aspects of the B-spline methodology on zonal grids.

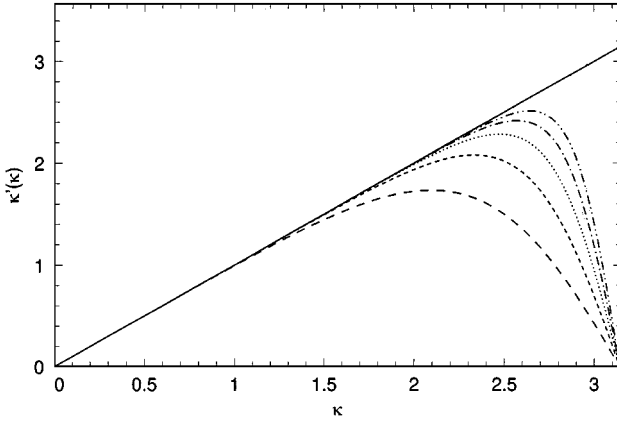


FIG. 9. Modified wave number diagram for first derivative operator in Galerkin method. —, spectral; B-splines of order ---, 1; ---, 2; ···, 3; —·—, 4; - - - , 5.

The equations considered in this test are

$$\frac{\partial u}{\partial t} + u \frac{\partial u}{\partial x} + v \frac{\partial u}{\partial y} = \nu \left(\frac{\partial^2}{\partial x^2} + \frac{\partial^2}{\partial y^2} \right) u, \tag{32a}$$

$$\frac{\partial v}{\partial t} + u \frac{\partial v}{\partial x} + v \frac{\partial v}{\partial y} = \nu \left(\frac{\partial^2}{\partial x^2} + \frac{\partial^2}{\partial y^2} \right) v, \tag{32b}$$

where the diffusion coefficient ν is chosen to be 0.03. Note that, for this test, the numerical approximations of the variables u and v in Eq. (32) are written in terms of B-spline functions that are not divergence-free

$$\tilde{u}(x, y) = \sum_{ij} \alpha_{ij}^{(u)} f_i(x) g_j(y), \tag{33a}$$

$$\tilde{v}(x, y) = \sum_{ij} \alpha_{ij}^{(v)} f_i(x) g_j(y). \tag{33b}$$

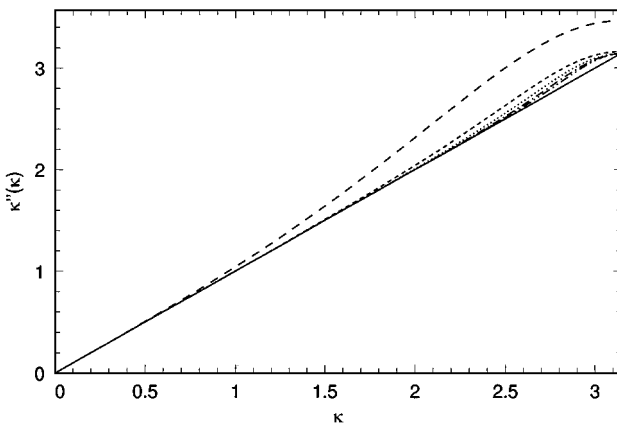


FIG. 10. Modified wave number diagram for second derivative operator in Galerkin method. —, spectral; B-splines of order ---, 1; ---, 2; ···, 3; —·—, 4; - - - , 5.

TABLE II

Summary of Numerical Parameters for 2D Nonlinear Convection-Diffusion Equation

Case	No. of zones	Grid spacing (min.; max.)	Total number of functions	Max. error
1	1	0.0048	44,521	—
2	1	0.0167	3,721	3.67×10^{-3}
3	8	(0.0167; 0.0667)	1,195	3.67×10^{-3}
4	1	0.0294	1,225	5.72×10^{-3}
5	8	(0.01; 0.04)	3,271	0.62×10^{-3}

The boundary conditions are

$$u(0, y) = v(0, y) = 1 - y, \quad (34a)$$

$$u(1, y) = v(1, y) = 1 - y, \quad (34b)$$

$$u(x, 0) = v(x, 0) = 1, \quad (34c)$$

$$u(x, 1) = v(x, 1) = 0. \quad (34d)$$

Equations (32) were solved in the domain $0 \leq x \leq 1$, $0 \leq y \leq 1$. All simulations were performed with the following initial conditions:

$$u(x, y) = v(x, y) = 1 - y.$$

The choice for initial conditions is not important because the solution is advanced in time to a steady state, where the results of different cases are compared. The test problem was solved on several multi-zone and single-zone grids. A summary of cases considered is shown in Table II. A constant time step $\Delta t = 0.01$ was used in all cases except in the base case 1, where $\Delta t = 0.005$ was used. In all cases, the maximum CFL number was always less than $\sqrt{3}$, which is required for stability of the third-order Runge–Kutta scheme.

The single-zone fine grid solution (case 1) was chosen as a base case against which the solutions for all other cases were compared. Errors for each solution were determined by computing an absolute value of the difference between the solution for this case and the base case solution. Initially, a single-zone simulation was performed (case 2) to locate regions of large errors. Based on this information, a zonal embedded grid was constructed in such a way that it had the same grid density in the region of the largest error as in case 2 but coarser elsewhere. Even though the errors in the fine zone were the same as in the same region of case 2, the errors in the coarse region were larger. These errors were especially large in the lower left corner of the domain. Due to the convective nature of the problem, the errors propagated towards the upper right corner of the domain. By refining a small region in the lower left corner (case 3), we were able to reduce these errors. Overall, the maximum errors of the solutions in cases 2 and 3 were approximately the same, but the solution in the latter case was obtained with the number of degrees of freedom almost three times smaller than in the former case. A single-zone solution (case 4) with the same number of degrees of freedom as in case 3 had errors that were almost two times larger than those of the zonal grid solution. Finally, case 5 had approximately the same number of degrees of freedom as case 2 but a finer grid in the region of the strong solution gradient (Fig. 11). The maximum error of the solution in this case was approximately six times smaller than that of the single-zone case 2. This was achieved primarily due to refining the important high gradient region at $x = 1$. The

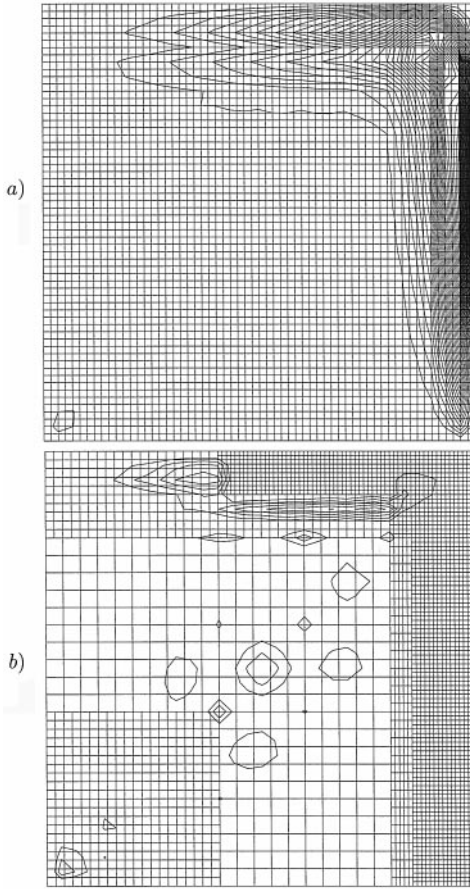


FIG. 11. Contours of error in the solution of nonlinear convection-diffusion equation: (a) case 2, single-zone grid, max error = 3.67×10^{-3} ; (b) case 5, multi-zone grid, max error = 0.62×10^{-3} . Contour interval in both cases is 10^{-4} .

rest of the domain had a relatively coarse grid as shown in Fig. 11. As a result, a more accurate solution was obtained without an increase in the computational cost. It is also important to note that there is no error accumulation near the region of sudden grid changes. There are some error contours observed near the upper right corner but they are mostly associated with the truncation errors in the solution and not with the zonal boundaries.

4.3. Laminar Flow over a Cylinder

Simulations of a laminar flow over a circular cylinder at two steady ($Re_D = 20$ and 40) and two unsteady ($Re_D = 80$ and 100) Reynolds numbers were performed. The Reynolds number is based on the free-stream velocity and the cylinder diameter. In each case, the simulations were initialized with potential flow and advanced in time until a stationary flow pattern was developed. At Reynolds numbers 20 and 40 , two attached vortices are formed behind the cylinder. The wake behind the cylinder at Reynolds numbers $Re_D = 80$ and 100 consists of negative and positive vortices shed alternately from the upper and the lower parts of the rear cylinder surface. An example of such a wake is given in Fig. 12 where the vorticity contours in the simulations at $Re_D = 100$ are shown. In our first simulations at unsteady Reynolds numbers, the onset of vortex shedding was induced by truncation and round-off errors that eventually break the symmetry of the numerical solution. However, this turned

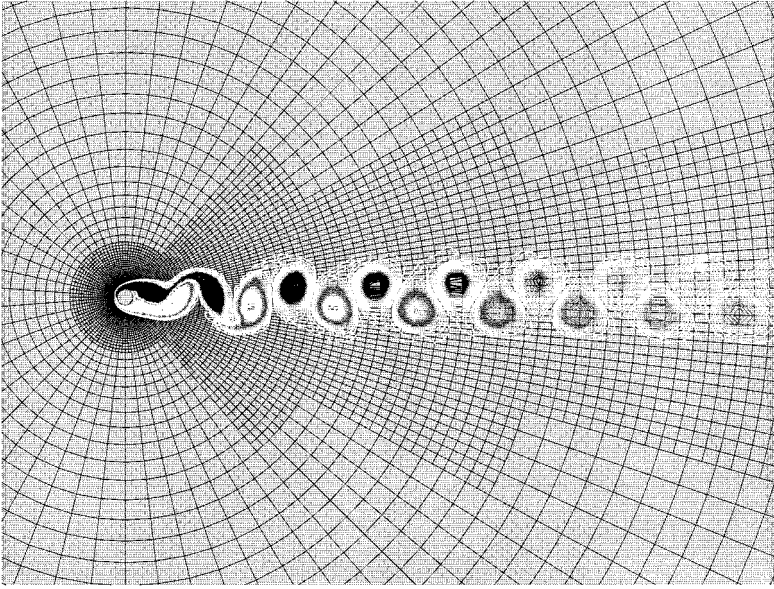


FIG. 12. Vortex shedding behind a circular cylinder at Reynolds number, $Re_D = U_\infty D/\nu = 100$, in simulations on zonal embedded grid. Vorticity contours, superimposed on the grid, are shown.

out to be a very slow process. The flow tended to stay symmetric up to $tU_\infty/D = 200$. In order to initiate vortex shedding, a time-dependent slip velocity on the cylinder was applied for a short period of time [25]. Thereafter, the flow was allowed to advance in time until all transient solutions exited the computational domain. Mean global quantities were recorded once a statistically steady flow pattern is formed.

Various flow quantities including pressure and viscous drag coefficients, mean length of the recirculation bubble, separation angle, and base pressure coefficient were computed and compared to the existing experimental and numerical results. At the unsteady Reynolds numbers, non-dimensional frequency of vortex shedding, the Strouhal number, and the amplitude of lift coefficients were also computed. Conventional definitions of the flow quantities were used,

$$C_{D_p} = \frac{1}{(1/2)\rho U_\infty^2 D} \int_0^{2\pi} P \cos \theta \, d\theta, \quad \text{pressure drag}$$

$$C_{D_v} = \frac{1}{(1/2)Re_D U_\infty} \int_0^{2\pi} \omega_w \sin \theta \, d\theta, \quad \text{viscous drag}$$

$$C_D = C_{D_p} + C_{D_v}, \quad \text{total drag}$$

$$C_{L_p} = \frac{1}{(1/2)\rho U_\infty^2 D} \int_0^{2\pi} P \sin \theta \, d\theta, \quad \text{pressure lift}$$

$$C_{L_v} = \frac{1}{(1/2)Re_D U_\infty} \int_0^{2\pi} \omega_w \cos \theta \, d\theta, \quad \text{viscous lift}$$

$$C_L = C_{L_p} + C_{L_v}, \quad \text{total lift}$$

$$St = fD/U_\infty, \quad \text{Strouhal number}$$

$$C_{P_b} = \frac{\bar{P}_b - P_\infty}{(1/2)\rho U_\infty^2}, \quad \text{base pressure,}$$

TABLE III
Summary of Cylinder Flow Computations at $Re_D = 100$

Case	R_d	k	N_r^{eff}	N_η^{eff}	C_D^{max}	C_L^{max}	$-C_{P_b}$	St	θ_{sep}	\bar{L}_{rec}	\bar{U}_{min}
1	20	2	78	81	1.405	0.350	0.891	0.167	117.0°	1.44	-0.188
2	30	2	84	81	1.370	0.301	0.879	0.165	117.0°	1.48	-0.189
3	30	3	86	163	1.304	0.286	0.728	0.163	117.4°	1.44	-0.173
4	40	2	89	177	1.286	0.311	0.710	0.162	117.3°	1.47	-0.176
5	40	3	92	163	1.308	0.318	0.735	0.163	117.4°	1.45	-0.175
6	60	2	96	177	1.294	0.311	0.713	0.162	117.3°	1.45	-0.173
7	60	3	104	163	1.312	0.313	0.738	0.164	117.4°	1.45	-0.175
8	80	2	102	81	1.296	0.330	0.723	0.164	117.4°	1.44	-0.175
9	80	2	102	161	1.296	0.318	0.723	0.164	117.4°	1.44	-0.175
10	80	3	102	81	1.301	0.313	0.725	0.164	117.4°	1.43	-0.173
11	90	3	122	163	1.314	0.314	0.739	0.164	117.4°	1.45	-0.175
12	120	2	116	81	1.312	0.316	0.733	0.164	117.4°	1.45	-0.175
13	120	2	202	161	1.314	0.314	0.735	0.164	117.4°	1.45	-0.175

Note. Overline indicates averaging in time. R_d is radius of computational domain, k is degree of B-splines. Other quantities are defined in the text.

where U_∞ is the uniform free-stream velocity, D is the diameter of the cylinder, f is the shedding frequency, ω_w is the wall vorticity, and P is the pressure. The separation angle, θ_{sep} , is defined at a point of zero wall vorticity. Mean length of the recirculation bubble (\bar{L}_{rec}) is non-dimensionalized by the cylinder diameter. The negative of the base pressure coefficient, a useful quantity, is usually called the base suction coefficient.

A series of simulations at $Re_D = 100$ were performed to establish grid and domain size independence. A summary of cases considered is shown in Table III. Domain sizes range from $R_d = 20$ to $R_d = 120$, where R_d is the radius of the domain in terms of the cylinder radius. The last six cases (cases 8–13) were performed on both single-zone and multi-zone grids. The effective number of grid points in the radial (N_r^{eff}) and circumferential (N_η^{eff}) directions are given in the table. The effective number of grid points is introduced to describe a zonal mesh and defined with respect to the corresponding single-zone mesh with the same resolution in the vicinity of the cylinder and in the wake. Normally, there are about 1.5–2.5 times less grid points in a multi-zone mesh than in a single-zone grid with the same near-cylinder resolution. The grid size in the radial direction at the cylinder surface was $\Delta r \sim 5 \times 10^{-3}$ for cases 1–12 and $\Delta r \sim 3.5 \times 10^{-3}$ for case 13. The grid was stretched in the radial direction with a hyperbolic tangent stretching function. The results from the table clearly show that the Strouhal number, separation angle, mean recirculation length, and mean minimum streamwise velocity (\bar{U}_{min}) become independent of the domain size when $R_d \geq 60$. Refining the grid in the circumferential and radial directions and increasing the degree of the B-splines do not affect the results significantly. Total drag and lift as well as base pressure coefficients appear to be more sensitive quantities especially for lower degree B-splines for which an even finer grid should be selected to achieve a better convergence.

The results of our simulations on the zonal grid of case 13 are shown in Figs. 13 and 14 together with the experimental results [26–28] and the numerical results from spectral calculations by Mittal [29] and spectral element simulations by Henderson [30]. Overall, the agreement between the present simulations and the existing results is good. There is a slight discrepancy between pressure drag coefficients obtained in our simulations and

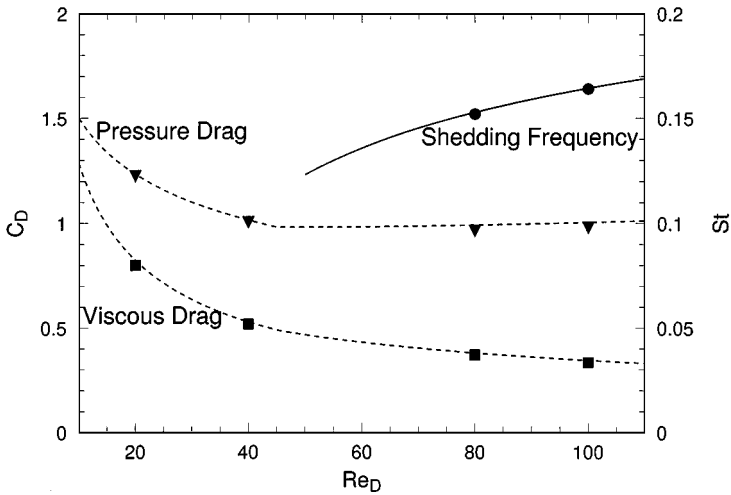


FIG. 13. Pressure and viscous drag and Strouhal number vs Reynolds number: —, experimental fit by Williamson [26]; ---, numerical fit by Henderson [30]; symbols, B-spline simulations.

those suggested by the numerical fit of Ref. [30]. However, the agreement between all other quantities is good.

4.4. Numerical Simulations of Flow over a Cylinder at $Re_D = 300$

The wake behind a circular cylinder becomes unstable to three-dimensional disturbances around $Re_D = 180$ – 200 [28] and develops large streamwise structures with spanwise wavelength of approximately 3–4 cylinder diameters. As the Reynolds number increases to around $Re_D = 260$, smaller three-dimensional structures with a spanwise wavelength of approximately one cylinder diameter become dominant. These structures are also known as mode-B instabilities [28]. With further increase in the Reynolds number, fine-scale

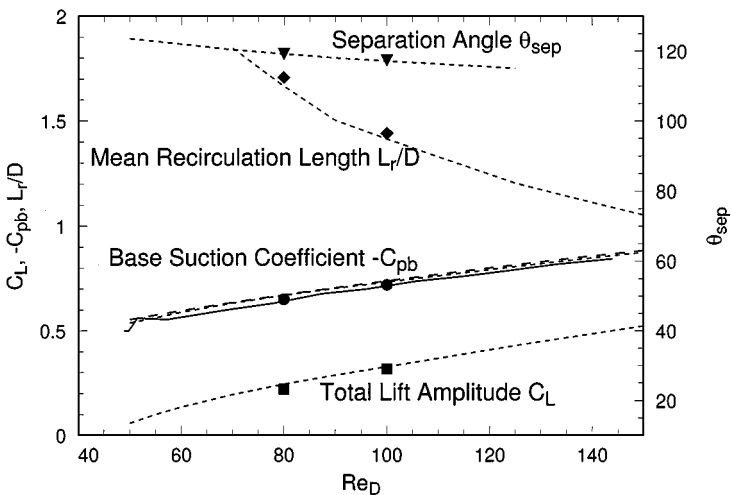


FIG. 14. Base suction coefficient, amplitude of total lift, mean recirculation length and separation angle vs Reynolds number: —, experimental data by Williamson and Roshko [27]; ---, numerical fits by Mittal [29]; ----, numerical fit by Henderson [30] (for base suction coefficient); symbols, B-spline simulations.

TABLE IV
Grid Parameters of Cylinder Flow Computations at $Re_D = 300$

Case	N_{zones}	N_r^{eff}	N_{BL} at $\theta = 170^\circ$	N_{BL} at $\theta = 90^\circ$	N_θ^{eff}	N_z	N_{total}	$R_d \times L_z$
1	4	91	6	10	103	48	369,120	$30D \times 2\pi D$
2	7	156	12	26	185	48	1,056,288	$30D \times 2\pi D$

Note. Parameters are N_{zones} , number of grid zones; N_r^{eff} and N_θ^{eff} , number of points in the radial and circumferential directions for corresponding single-zone grid; N_z , number of points in spanwise direction; N_{BL} , number of points in boundary layer; N_{total} , total number of grid points; R_d , domain radius; L_z , spanwise domain size.

three-dimensional structures become more and more active. Flow over a cylinder at Reynolds number, $Re_D = 300$, which belongs to this regime, was chosen for our study. Relatively low Reynolds number, availability of previous computational and experimental data, and the presence of small and large three-dimensional structures make this flow an interesting and yet not a computationally demanding test to assess the performance of the three-dimensional version of the B-spline method on zonal grids. This flow has been studied computationally by Mittal and Balachandar [25] who used a spectral method on an O-type cylindrical grid. That study is used as a reference for our simulations.

Two simulations of the flow over a cylinder at $Re_D = 300$ were carried out with different grid resolutions. The grid parameters for the two cases are summarized in Table IV. The total number of grid points is approximately 3 times larger in case 2 than in case 1. The grids of cases 1 and 2 make use of zonal grid embedding and grid stretching in both the radial and circumferential directions. Our reference case, simulations of Mittal and Balachandar [25], had the O-type mesh with $N_r \times N_\theta \times N_z = 81 \times 160 \times 288$ grid points. Because Mittal and Balachandar [25] used spectral methods, their grid was uniform in the spanwise and circumferential directions and stretched with a cosine function in the radial direction. The radius of the domain in the calculations of Mittal and Balachandar [25] was $15D$ and the spanwise domain was $L_z \sim 10.8D$. The grid in case 1 is coarser in the circumferential direction but comparable in the radial direction at the cylinder to that in the simulations of Mittal and Balachandar [25]. The grid resolution in case 2 is about two times finer in the radial direction in the vicinity of the cylinder.

Two important flow features should be considered when designing a grid for computations of the flow over a cylinder: the thickness of the boundary layer and the size of the dominant streamwise vortical structures in the wake. The thickness of the boundary layer is estimated *a posteriori* from the size of the vorticity layer at the cylinder surface. The number of grid points in the boundary layer on the cylinder at $\theta = 170^\circ$ and $\theta = 90^\circ$ ($\theta = 0^\circ$ is at the base of the cylinder and $\theta = 180^\circ$ is at the front stagnation point) is given in Table IV. Case 2 has two times more grid points in the boundary layer than case 1. As reported in the experimental studies by Williamson [28], the estimated spanwise length scale of the streamwise vortices at $Re_D = 300$ is $\lambda_z \sim D$. Mittal and Balachandar [25] found that simulations of flow over a cylinder at $Re_D = 300$ are very sensitive to the size of the spanwise computational domain and showed variations in the mean flow parameters such as drag and lift coefficients, Strouhal shedding frequency, and base suction coefficient, when different spanwise domains were used. The prediction of mean flow quantities improved on a larger spanwise domain. Following that study, we chose the spanwise domain for our calculations to be $2\pi D$.

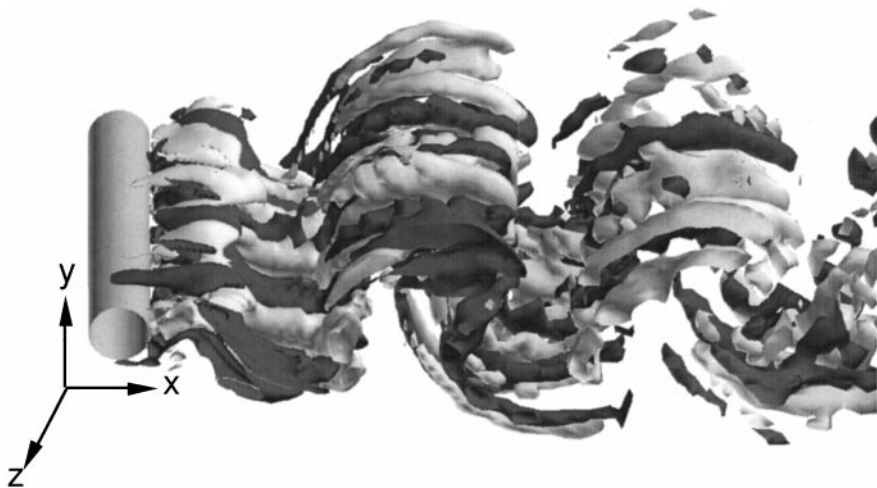


FIG. 15. Isosurfaces of instantaneous streamwise vorticity in the wake of a circular cylinder at $Re_D = 300$: light, $\omega_x D/U_\infty = .24$; dark, $\omega_x D/U_\infty = -.24$; three-dimensional view.

The code for the computations was compiled and executed on Cray C90 in vectoral mode and on SGI Origin 2000 in parallel mode. It was able to achieve the performance of around 4×10^{-5} s per grid point per time step on Cray C90.

Coarse grid simulations were initialized with the potential flow solution and advanced in time until a statistically steady flow pattern was developed. Fine grid simulations were initialized with a velocity field interpolated from the coarse grid calculations. Once the three-dimensional wake was developed, both simulations were advanced in time for approximately 12 shedding cycles ($T \sim 60D/U_\infty$) to ensure the removal of initial transients. The statistics of the mean flow quantities were then accumulated for 8 more shedding cycles ($T \sim 40D/U_\infty$).

Figures 15 and 16 show perspective and bottom (x - z plane) views, respectively, of the instantaneous streamwise vorticity iso-surfaces. The flow is from left to right. The figures clearly show the development of the pattern associated with the Karman vortex street and



FIG. 16. The same conditions as Fig. 15 but x - z plane view.

TABLE V
Flow Parameters of Cylinder Flow Computations at $Re_D = 300$

Case	\bar{C}_D	$\bar{C}_{L_{rms}}$	$-C_{p_b}$	St
Spectral ^a	1.26	0.38	0.99	0.203
Experiment	1.22	—	0.96	0.203
1	1.24	0.33	0.90	0.202
2	1.28	0.40	1.01	0.203

Note. Experimental St and $-C_{p_b}$ are from Ref. [28]; C_D from Ref. [31].

^a Simulations by Mittal and Balachandar [25].

the presence of mode-B streamwise vortices which were also observed in other numerical [32, 33] and experimental [33–35] studies. Even though the dominant structures in the near-wake are the counter-rotating streamwise vortices, they appear to vary in size and strength. A highly complex evolution of these structures have been also observed in the previous numerical simulations [32, 36]. Farther downstream, the number of the streamwise vortical structures seems to decrease, which is also consistent with the observations of Mittal and Balachandar [32].

Mean flow parameters are summarized in Table V. All statistical quantities are averaged both in time and across the cylinder span and non-dimensionalized with respect to the free-stream velocity, U_∞ , and the cylinder diameter, D . The overall agreement between the B-spline computations, the spectral results, and experimental data is good. The small differences are attributed to insufficient time-averaging. The flow is believed to have large time scales that require prohibitively large computer resources to obtain a sufficient statistical sample [32].

Figures 17 and 18 show the mean velocity profiles from coarse and fine grid simulations at five downstream locations in the near-wake of the cylinder. The B-spline simulations are compared to the results of spectral computations [32]. The intensities of velocity fluctuations and Reynolds shear stress are shown in Figs. 19–21. The profiles of both mean velocities

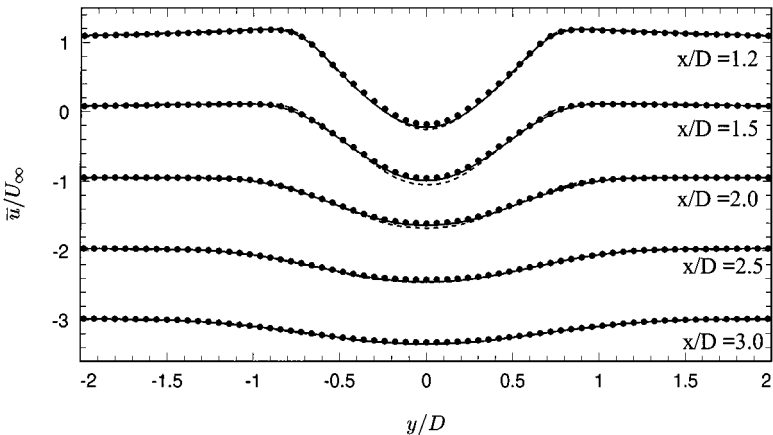


FIG. 17. Mean streamwise velocity at different locations in the wake of a circular cylinder at $Re_D = 300$: —, B-spline simulations on fine grid; ---, B-spline simulations on coarse grid; •, spectral simulations by Mittal and Balachandar [32].

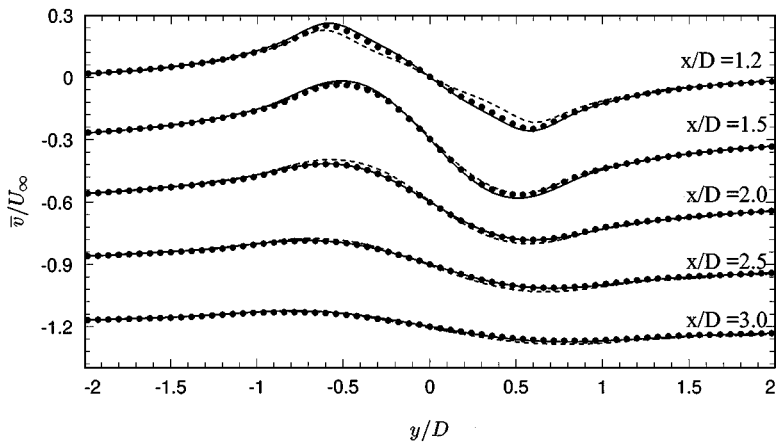


FIG. 18. Mean crossflow velocity at different locations in the wake of a circular cylinder at $Re_D = 300$. See caption for Fig. 17.

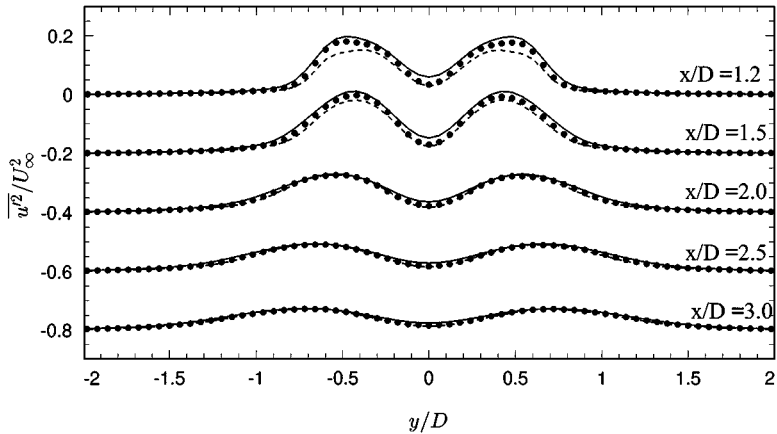


FIG. 19. Time-averaged streamwise velocity fluctuations at different locations in the wake of a circular cylinder at $Re_D = 300$. See caption for Fig. 17.

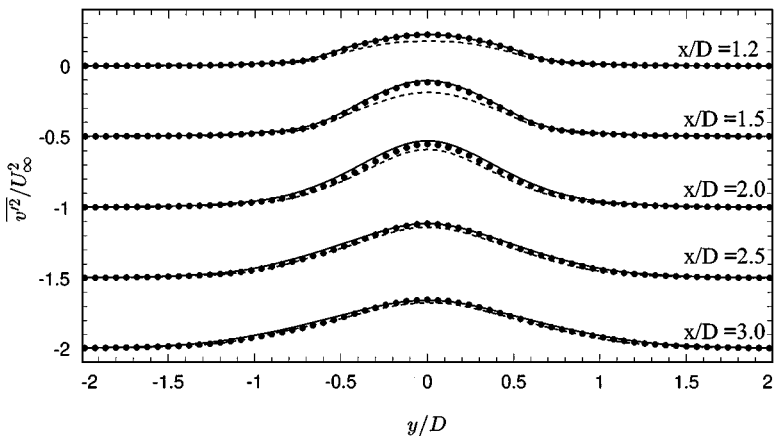


FIG. 20. Time-averaged crossflow velocity fluctuations at different locations in the wake of a circular cylinder at $Re_D = 300$. See caption for Fig. 17.

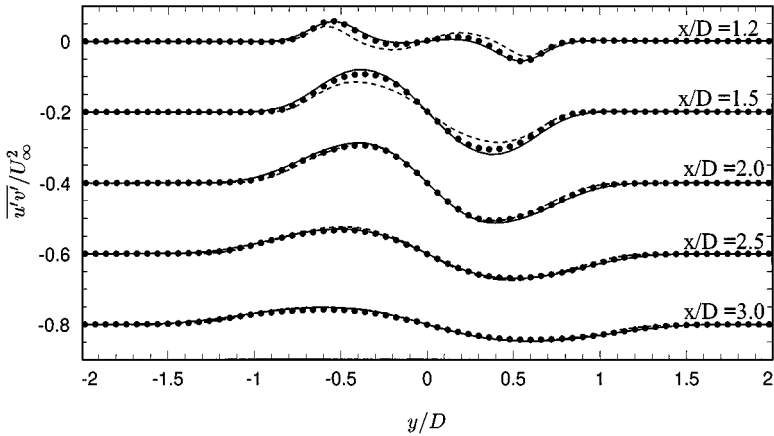


FIG. 21. Time-averaged Reynolds shear stress at different locations in the wake of a circular cylinder at $Re_D = 300$. See caption for Fig. 17.

and velocity fluctuations show excellent agreement between the fine B-spline and spectral computations. The coarse grid simulations are slightly off but the differences are small and there is a convergence of the profiles with grid refinement.

5. CONCLUSIONS

There is a need for the development of high-order non-dissipative schemes for simulations of turbulent flows in geometries more complex than those treated by spectral methods. It was demonstrated that a numerical method based on B-splines appears to be an attractive alternative to high-order finite-difference schemes. The method is accurate, non-dissipative, and free of aliasing errors. The method is also promising for computations on zonal embedded grids which are necessary for large eddy simulations of wall-bounded flows. In such flows, a fine grid is required in all three directions near the walls to resolve important turbulent structures (large eddies) that are small compared to the overall flow dimensions. An efficient resolution of these structures can be achieved with zonal grids. Zonal grids are also necessary for LES of complex separated flows with thin shear layers.

The B-spline method developed in this paper is based on divergence-free B-spline functions and is designed for simulations of turbulent flows in complex geometries. The method employs zonal grids and permits fine meshes to be embedded in physically significant flow regions without placing a large number of grid points in the rest of the computational domain.

The method was successfully tested in numerical solutions of nonlinear advection-diffusion equations. The tests indicated that the method provides for an efficient information transfer between zones without accumulation of errors in the regions of sudden grid changes.

The performance of the numerical method was also assessed in simulations of laminar flows over a circular cylinder at low Reynolds numbers. The lift, drag, and base suction coefficients, the size of the recirculation bubble, and the vortex shedding frequency agree well with the experimental data and previous simulations of these flows. The numerical solutions on multi-zonal grids are of the same accuracy as those on a single-zone grid but require less computer resources. Three-dimensional numerical simulations of flow over a cylinder at $Re_D = 300$ show good agreement with the corresponding spectral calculations

in terms of velocity profiles in the wake. Coefficient of drag and the Strouhal shedding frequency agree well with the experimental data.

APPENDIX

A.1. Mass Matrices

Mass matrices in (9) are given by

$$\mathbf{M}^{\pm\pm} = \int_{\Omega} \boldsymbol{\psi}^{\pm} \cdot \mathbf{q}^{\pm} J d\xi d\eta.$$

Therefore,

$$\begin{aligned} \mathbf{M}^{++} &= \int_0^1 \int_0^1 (a^2 + b^2) J d\xi d\eta, \\ \mathbf{M}^{+-} &= \int_0^1 \int_0^1 ik_z (c_a a + c_b b) J d\xi d\eta, \\ \mathbf{M}^{-+} &= \int_0^1 \int_0^1 -ik_z (c_a a + c_b b) J d\xi d\eta, \\ \mathbf{M}^{--} &= \int_0^1 \int_0^1 -k_z^2 (c_a^2 + c_b^2) + d^2 J d\xi d\eta. \end{aligned}$$

A.2. Viscous Matrices

Viscous matrices in (9) are given by

$$\mathbf{D}^{\pm\pm} = \int_{\Omega} \nabla \times \boldsymbol{\psi}^{\pm} \cdot \nabla \times \mathbf{q}^{\pm} J d\xi d\eta.$$

Using definitions for $\boldsymbol{\psi}^{\pm}$ and \mathbf{q}^{\pm} , we obtain

$$\begin{aligned} \mathbf{D}^{++} &= \int_0^1 \int_0^1 [k_z^2 (a^2 + b^2) J^2 + [a_{\xi} x_{\eta} - a_{\eta} x_{\xi} + b_{\xi} y_{\eta} - b_{\eta} y_{\xi}]^2] \frac{1}{J} d\xi d\eta, \\ \mathbf{D}^{+-} &= \int_0^1 \int_0^1 \left[ik_z \left[b(d_{\eta} x_{\xi} - d_{\xi} x_{\eta}) - a(d_{\eta} y_{\xi} - d_{\xi} y_{\eta}) \right. \right. \\ &\quad \left. \left. + \frac{1}{J} (a_{\xi} x_{\eta} - a_{\eta} x_{\xi} + b_{\xi} y_{\eta} - b_{\eta} y_{\xi}) (c_{a\xi} x_{\eta} - c_{a\eta} x_{\xi} + c_{b\xi} y_{\eta} - c_{b\eta} y_{\xi}) \right] \right. \\ &\quad \left. + ik_z^3 (ac_a + bc_b) J \right] d\xi d\eta, \\ \mathbf{D}^{-+} &= \int_0^1 \int_0^1 \left[-ik_z \left[(d_{\eta} x_{\xi} - d_{\xi} x_{\eta}) b - (d_{\eta} y_{\xi} - d_{\xi} y_{\eta}) a \right. \right. \\ &\quad \left. \left. + \frac{1}{J} (c_{a\xi} x_{\eta} - c_{a\eta} x_{\xi} + c_{b\xi} y_{\eta} - c_{b\eta} y_{\xi}) (a_{\xi} x_{\eta} - a_{\eta} x_{\xi} + b_{\xi} y_{\eta} - b_{\eta} y_{\xi}) \right] \right. \\ &\quad \left. - ik_z^3 (c_a a + c_b b) J \right] d\xi d\eta, \end{aligned}$$

$$\begin{aligned}
\mathbf{D}^{-} = & \int_0^1 \int_0^1 [(d_\eta x_\xi - d_\xi x_\eta)^2 + (d_\eta y_\xi - d_\xi y_\eta)^2 \\
& + k_z^2 [c_{a\xi} x_\eta - c_{a\eta} x_\xi + c_{b\xi} y_\eta - c_{b\eta} y_\xi]^2 \\
& + k_z^2 [c_a J(d_\eta y_\xi - d_\xi y_\eta) + J(d_\eta y_\xi - d_\xi y_\eta) c_a \\
& + c_b J(d_\eta x_\xi - d_\xi x_\eta) + J(d_\eta x_\xi - d_\xi x_\eta) c_b] + k_z^4 J^2 (c_a^2 + c_b^2)] \frac{1}{J} d\xi d\eta.
\end{aligned}$$

A.3. Nonlinear Terms

Before computation of the nonlinear terms, we transform the coefficients in the velocity expansions (1) from Fourier to physical space:

$$\begin{aligned}
\hat{\alpha}^+(t, k_z) &\rightarrow \alpha^+(t, z), \\
\hat{\alpha}^-(t, k_z) &\rightarrow \alpha^-(t, z).
\end{aligned}$$

In physical space, the velocity vector is given by

$$\mathbf{u} = \sum_{n,m} \alpha^+(t, z) \begin{pmatrix} a(\xi, \eta) \\ b(\xi, \eta) \\ 0 \end{pmatrix} + \begin{pmatrix} \alpha_z^-(t, z) c_a(\xi, \eta) \\ \alpha_z^-(t, z) c_b(\xi, \eta) \\ \alpha^-(t, z) d(\xi, \eta) \end{pmatrix},$$

where the subscript in α_z indicates differentiation with respect to z . Let us decompose the weight vectors, $\psi^+(\xi, \eta, z)$ and $\psi^-(\xi, \eta, z)$, as

$$\psi^+(\xi, \eta, z) = [\psi \mathbf{1}^+(\xi, \eta)] e^{-ik_z z}, \quad \psi^-(\xi, \eta, z) = [\psi \mathbf{1}^-(\xi, \eta) - ik_z \psi \mathbf{2}^-(\xi, \eta)] e^{-ik_z z},$$

where

$$\psi \mathbf{1}^+(\xi, \eta) = \begin{pmatrix} a(\xi, \eta) \\ b(\xi, \eta) \\ 0 \end{pmatrix}, \quad \psi \mathbf{1}^-(\xi, \eta) = \begin{pmatrix} 0 \\ 0 \\ d(\xi, \eta) \end{pmatrix}, \quad \psi \mathbf{2}^-(\xi, \eta) = \begin{pmatrix} c_a(\xi, \eta) \\ c_b(\xi, \eta) \\ 0 \end{pmatrix}.$$

Then, the nonlinear terms are

$$N_1^+ = \int_0^1 \int_0^1 \psi 1_{i_{pl}}^+ [(y_\eta u_i u)_\xi - (x_\eta u_i v)_\xi - (y_\xi u_i u)_\eta + (x_\xi u_i v)_\eta] d\xi d\eta,$$

$$N_2^+ = \int_0^1 \int_0^1 \psi 1_{i_{pl}}^+ (u_i w) J d\xi d\eta,$$

$$N_1^- = \int_0^1 \int_0^1 \psi 1_{i_{pl}}^- [(y_\eta u_i u)_\xi - (x_\eta u_i v)_\xi - (y_\xi u_i u)_\eta + (x_\xi u_i v)_\eta] d\xi d\eta,$$

$$N_2^- = \int_0^1 \int_0^1 \psi 2_{i_{pl}}^- [(y_\eta u_i u)_\xi - (x_\eta u_i v)_\xi - (y_\xi u_i u)_\eta + (x_\xi u_i v)_\eta] + \psi 1_{i_{pl}}^- (u_i w) d\xi d\eta,$$

$$N_3^- = \int_0^1 \int_0^1 \psi 2_{i_{pl}}^- (u_i w) J d\xi d\eta.$$

These expressions can be re-written in terms of expansion coefficients α^+ and α^- as

$$\begin{aligned}\mathbf{N}_1^+ &= N1_1^+ \alpha^+ \alpha^+ + N2_1^+ \alpha^+ \alpha_z^- + N3_1^+ \alpha_z^- \alpha_z^-, \\ \mathbf{N}_2^+ &= N1_2^+ \alpha^+ \alpha^- + N2_2^+ \alpha_z^+ \alpha^-, \\ \mathbf{N}_1^- &= N1_1^- \alpha^+ \alpha^- + N2_1^- \alpha_z^+ \alpha^-, \\ \mathbf{N}_2^- &= N1_2^- \alpha^+ \alpha^+ + N2_2^- \alpha^+ \alpha_z^- + N3_2^- \alpha_z^- \alpha_z^- + N4_2^- \alpha^- \alpha^-, \\ \mathbf{N}_3^- &= N1_3^- \alpha^+ \alpha^- + N2_3^- \alpha_z^- \alpha^-, \end{aligned}$$

where

$$\begin{aligned}\mathbf{N1}_1^+ &= \int_0^1 \int_0^1 [(a_\eta y_\xi - a_\xi y_\eta)aa + (b_\xi x_\eta - b_\eta x_\xi)bb \\ &\quad + (a_\xi x_\eta - a_\eta x_\xi + b_\eta y_\xi - b_\xi y_\eta)ab] d\xi d\eta, \\ \mathbf{N2}_1^+ &= \int_0^1 \int_0^1 [2(a_\eta y_\xi - a_\xi y_\eta)ac_a + (a_\xi x_\eta - a_\eta x_\xi + b_\eta y_\xi - b_\xi y_\eta)(ac_b + bc_a) \\ &\quad + 2(b_\xi x_\eta - b_\eta x_\xi)bc_b] d\xi d\eta, \\ \mathbf{N3}_1^+ &= \int_0^1 \int_0^1 [(a_\eta y_\xi - a_\xi y_\eta)c_a c_a (b_\xi x_\eta - b_\eta x_\xi)c_b c_b] d\xi d\eta, \\ \mathbf{N1}_2^+ &= \int_0^1 \int_0^1 [aad + bbd]J d\xi d\eta, \\ \mathbf{N2}_2^+ &= \int_0^1 \int_0^1 [ac_a d + bc_b d]J d\xi d\eta, \\ \mathbf{N1}_1^- &= \int_0^1 \int_0^1 [(d_\eta y_\xi - d_\xi y_\eta)ad + (d_\xi x_\eta - d_\eta x_\xi)bd] d\xi d\eta, \\ \mathbf{N2}_1^- &= \int_0^1 \int_0^1 [(d_\xi x_\eta - d_\eta x_\xi)c_a d + (d_\xi x_\eta - d_\eta x_\xi)c_b d] d\xi d\eta, \\ \mathbf{N1}_2^- &= \int_0^1 \int_0^1 [(-c_{a\eta} x_\xi + c_{a\xi} x_\eta)ab + (-c_{a\xi} y_\eta + c_{a\eta} y_\xi)bb \\ &\quad + (c_{b\eta} y_\xi - c_{b\xi} y_\eta)ab + (c_{b\xi} x_\eta - c_{b\eta} x_\xi)bb] d\xi d\eta, \\ \mathbf{N2}_2^- &= \int_0^1 \int_0^1 [(-c_{a\eta} x_\xi + c_{a\xi} x_\eta)ac_a + 2(-c_{a\xi} y_\eta + c_{a\eta} y_\xi)ac_a \\ &\quad + (c_{b\eta} y_\xi - c_{b\xi} y_\eta)ac_b + 2(c_{b\xi} x_\eta - c_{b\eta} x_\xi)bc_b] d\xi d\eta, \\ \mathbf{N3}_2^- &= \int_0^1 \int_0^1 [(-c_{a\xi} y_\eta + c_{a\eta} y_\xi)c_a c_a + (c_{b\xi} x_\eta - c_{b\eta} x_\xi)c_b c_b \\ &\quad + (-c_{b\xi} y_\eta + c_{b\eta} y_\xi + c_{a\xi} x_\eta - c_{a\eta} x_\xi)c_a c_b] d\xi d\eta, \\ \mathbf{N4}_2^- &= \int_0^1 \int_0^1 [-ddd]J d\xi d\eta, \end{aligned}$$

$$\mathbf{N1}_3^- = \int_0^1 \int_0^1 [c_a a d + c_b b d] J d\xi d\eta,$$

$$\mathbf{N2}_3^- = \int_0^1 \int_0^1 [c_a c_a d + c_b c_b d] J d\xi d\eta.$$

Each of the expressions above is a multi-indexed quantity of the form N_{ijklmn} and size $\sim N_\xi \times N_\eta \times (2k+1)^4$ discussed above. These so-called nonlinear matrices are pre-computed and stored before the time advancement. Once the nonlinear terms are evaluated, they are transformed back to Fourier space,

$$\mathbf{N}_i^\pm(t, z) \rightarrow \hat{\mathbf{N}}_i^\pm(t, k_z),$$

and we obtain expressions for the nonlinear parts of the RHSs of our system of Eqs. (9),

$$\begin{aligned} \hat{\mathbf{R}}^+(\alpha^+, \alpha^-) &= \hat{\mathbf{N}}_1^+ + ik_z \hat{\mathbf{N}}_2^+ \\ \hat{\mathbf{R}}^-(\alpha^+, \alpha^-) &= \hat{\mathbf{N}}_1^- - ik_z \hat{\mathbf{N}}_2^- + k_z^2 \hat{\mathbf{N}}_3^-. \end{aligned}$$

ACKNOWLEDGMENTS

The financial support of this work by the Office of Naval Research under Grant N0014-94-1-0165 (with Dr. P. Purtell as project manager) is gratefully acknowledged. The computer resources are provided by the computer facilities of NASA Ames Research Center. We thank Dr. Robert Moser for many useful discussions.

REFERENCES

1. P. Moin and J. Jimenez, Large eddy simulation of complex turbulent flows, in *AIAA 24th Fluid Dynamics Conference, Orlando, FL, July 6-9, 1993*, paper AIAA-93-3099, 1993.
2. J. W. Deardorff, A numerical study of three-dimensional turbulent channel flow at large Reynolds numbers, *J. Fluid Mech.* **41**, 453 (1970).
3. U. Schumann, Subgrid scale model for finite-difference simulations of turbulent flows in plane channels and annuli, *J. Comput. Phys.* **18**, 376 (1975).
4. W. Cabot, Large eddy simulations with wall models, in *CTR Annual Research Briefs* (Center for Turbulence Research, NASA-Ames/Stanford University, 1995), p. 41.
5. M. M. Rai, An implicit, conservative, zonal-boundary scheme for Euler equation calculations, *Comput. & Fluids* **14**(3), 295 (1986).
6. M. M. Rai and P. Moin, Direct numerical simulation of transition and turbulence in a spatially evolving boundary layer, *J. Comput. Phys.* **109**, 169 (1993).
7. Y. Kallinderis, Numerical treatment of grid interfaces for viscous flows, *J. Comput. Phys.* **98**, 129 (1992).
8. Y. Zang and R. L. Street, A composite multigrid method for calculating unsteady incompressible flows in geometrically complex domains, *Int. J. Numer. Methods Fluids* **20**, 341 (1995).
9. J. Y. Tu and L. Fuchs, Overlapping grids and multigrid methods for three-dimensional unsteady flow calculations in IC engines, *Int. J. Numer. Methods Fluids* **15**, 693 (1992).
10. P. P. Sullivan, J. C. McWilliams, and C.-H. Moeng, A grid nesting method for large-eddy simulation of planetary boundary layers, *Boundary-Layer Meteorol.* **80**, 167 (1996).
11. B. J. Boersma, M. N. Kooper, F. T. Nieuwstadt, and P. Wesseling, Local grid refinement in large eddy simulations, *J. Eng. Math.* **32**, 161 (1997).
12. S. Ghosal, An analysis of numerical errors in large eddy simulations of turbulence, *J. Comput. Phys.* **125**, 187 (1996).

13. T. Lund and H.-J. Kaltenbach, Experiments with explicit filtering for LES using finite-difference methods, in *CTR Annual Research Briefs* (Center for Turbulence Research, NASA-Ames/Stanford University, 1995), p. 91.
14. A. G. Kravchenko and P. Moin, On the effect of numerical errors in large eddy simulations of turbulent flows, *J. Comput. Phys.* **131**, 310 (1997).
15. F. H. Harlow and J. E. Welch, Numerical calculation of time-dependent viscous incompressible flow of fluid with free-surface, *Phys. Fluids* **8**, 2182 (1965).
16. J. Kim and P. Moin, Application of a fractional-step method to incompressible Navier–Stokes equations, *J. Comput. Phys.* **59**, 308 (1985).
17. Y. Morinishi, Conservative properties of finite-difference schemes for incompressible flow, in *CTR Annual Research Briefs* (Center for Turbulence Research, NASA-Ames/Stanford University, 1995), p. 121.
18. A. G. Kravchenko, P. Moin, and R. Moser, Zonal embedded grids for numerical simulations of wall-bounded turbulent flows, *J. Comput. Phys.* **127**, 412 (1996).
19. K. Shariff and R. D. Moser, Two-dimensional mesh embedding for B-spline methods, *J. Comput. Phys.* **145**, 471 (1998).
20. A. Leonard and A. Wray, A new numerical method for simulation of three-dimensional flow in a pipe, in *Proceedings of International Conference on Numerical Methods in Fluid Dynamics, 8th Aachen*, edited by E. Krause, Lecture Notes in Physics (Springer-Verlag, New York, 1982), Vol. 170, p. 335.
21. C. de Boor, *A Practical Guide to Splines* (Springer-Verlag, Berlin, 1978).
22. S. A. Orszag, On the elimination of aliasing in finite-difference schemes by filtering high-wavenumber components, *J. Atmosph. Sci.* **28**, 1074 (1971).
23. G. Strang and G. J. Fix, *An Analysis of the Finite Element Method* (Prentice Hall, Englewood Cliffs, NJ, 1973).
24. S. Lele Compact finite-difference schemes with spectral-like resolution, *J. Comput. Phys.* **103**, 16 (1992).
25. R. Mittal, and S. Balachandar, Effect of three-dimensionality on the lift and drag of nominally two-dimensional cylinders, *Phys. Fluids* **7**(8), 1841 (1995).
26. C. H. K. Williamson, Defining a universal and continuous Strouhal–Reynolds number relationship for the laminar vortex shedding of a circular cylinder, *Phys. Fluids* **31**, 2742 (1988).
27. C. H. K. Williamson and A. Roshko, Measurements of base pressure in the wake of a cylinder at low Reynolds numbers, *Z. Flugwiss. Weltraumforsch* **14**, 38 (1990).
28. C. H. K. Williamson, Vortex dynamics in the cylinder wake, *Annu. Rev. Fluid. Mech.* **28**, 477 (1996).
29. R. Mittal, private communication, 1996.
30. R. D. Henderson, Details of the drag curve near the onset of vortex shedding, *Phys. Fluids* **7**(9), 2102 (1995).
31. C. Wieselsberger, *New Data on the Laws of Fluid Resistance*, Report NACA-TN-84, 1922.
32. R. Mittal and S. Balachandar, On the inclusion of three-dimensional effects in simulations of two-dimensional bluff body wake flows, in *Proceedings of ASME Fluids Engineering Division Summer Meeting, Vancouver, British Columbia, Canada, June 22–26, 1997*, available on CD-ROM only, 1997.
33. H.-Q. Zhang, Y. Fey, and B. R. Noack, On the transition of the cylinder wake, *Phys. Fluids* **7**(4), 779 (1995).
34. C. H. K. Williamson, The natural and forced formation of spot-like “vortex dislocations” in the transition of a wake, *J. Fluid Mech.* **243**, 393 (1992).
35. C. H. K. Williamson, Three-dimensional wake transition behind a cylinder, *J. Fluid Mech.* **328**, 345 (1996).
36. M. Thompson, K. Hourigan, and J. Sheridan, Three-dimensional instabilities in the wake of a circular cylinder, *Exper. Thermal Fluid Sci.* **12**(2), 190 (1996).